

Planetary Nebulae Kinematics in M31

Denise Hurley-Keller^{1,2}, Heather L. Morrison³, & Paul Harding¹

Astronomy Department, Case Western Reserve University, 10900 Euclid Ave. Cleveland, OH 44106; denise@smaug.astr.cwru.edu, heather@vegemite.astr.cwru.edu, harding@dropbear.astr.cwru.edu

George H. Jacoby

WIYN Observatory, P.O. Box 26732, Tucson, AZ 85726; jacoby@wiyn.org

ABSTRACT

We present kinematics of 135 planetary nebulae in M31 from a survey covering 3.9 deg^2 and extending out to 15 kpc from the southwest major axis and more than 20 kpc along the minor axis. The majority of our sample, even well outside the disk, shows significant rotational support (mean line-of-sight velocity 116 km/s). We argue that these PN belong to the outer part of M31's large $R^{1/4}$ bulge. Only five PN have velocities clearly inconsistent with this fast rotating bulge. All five may belong to tidal streams in M31's outer halo. One is projected on the Northern Spur, and is counter-rotating with respect to the disk there. Two are projected near the major axis at $X = -10$ kpc and have M32-like velocities; they could be debris from that galaxy. The remaining two halo PN are located near the center of the galaxy and their velocities follow the gradient found by Ibata et al. (2004), implying that these PN could belong to the Southern Stream. If M31 has a non-rotating, pressure-supported halo, we have yet to find it, and it must be a very minor component of the galaxy.

Subject headings: galaxies: kinematics and dynamics — galaxies: stellar content — galaxies: individual (M31) — galaxies: halos

¹Visiting Astronomer, Kitt Peak National Observatory, National Optical Astronomy Observatory, which is operated by the Association of Universities for Research in Astronomy, Inc. (AURA) under cooperative agreement with the National Science Foundation.

²NSF Astronomy & Astrophysics Postdoctoral Fellow

³Cottrell Scholar of Research Corporation and NSF CAREER fellow

1. Introduction

The wealth of information resulting from highly detailed studies of the old stellar populations of the Galaxy (Eggen, Lynden-Bell, & Sandage 1962; Searle & Zinn 1978; Gilmore & Reid 1983; Edvardsson et al. 1993) have been a catalyst for theories of galaxy evolution; as the nearest large galaxy to us, M31 is a proving ground for those theories. M31 offers a variety of stellar populations in a galaxy of earlier Hubble type, providing important leverage in testing formation scenarios. Especially important are the faint, old populations of the halo, which have proven difficult to study directly in more distant galaxies (Morrison 1999; Zepf et al. 2000). Halos contain the first stars, and the ages and abundances of these stars reflect the properties of the protogalactic fragments that are the building blocks of galaxies (e.g. Oey 2000). The kinematics of halo populations tells us about the dynamical evolution of the galaxy, and provide constraints on hierarchical formation theories (Helmi et al. 1999; Ivezić et al. 2000; Yanny et al. 2000; Dohm-Palmer et al. 2001).

How can we describe M31’s old populations? What can their properties tell us about how M31 formed and evolved? The old stellar populations in the Milky Way have often been used as a guide to these populations in other disk galaxies because of the richness of spatial and velocity data for the Milky Way. In the Milky Way, the metal-poor, old stars of the halo dominate a few kpc away from the plane and the galactic center. The field stars and globular clusters have a power-law density profile (Zinn 1985; Saha 1985; Ivezić et al. 2000) and pressure-supported kinematics with little or no rotation (also see Beers et al. 2000, for a recent summary of halo kinematics in the Milky Way).

This density profile differs from that of M31’s spheroid, which has an $R^{1/4}$ profile extending unchanged for a remarkably large distance along the minor axis (20 kpc, Pritchet & van den Bergh 1994; hereafter PvdB; 30 kpc, Durrell, Harris, & Pritchet 2004). Color-magnitude diagram studies of red giants have shown that, although there is a weak (10–20%) metal-poor component, the dominant stellar population at these halo-like distances is about 1 dex more metal-rich than its Milky Way counterpart, or than the M31 globular clusters at the same radius (Mould & Kristian 1986; Durrell, Harris, & Pritchet 1994; Couture et al. 1995; Rich et al. 1996; Durrell, Harris, & Pritchet 2001). This led Mould (1986) and Freeman (1996) to suggest that the bulge dominates even at these very large distances from the galactic center.

The Milky Way’s bulge is quite different. It is less luminous and its inner 1-2 kpc are dominated by a bar, which has a vertical exponential distribution with scale height of around 350 pc (Weiland et al. 1994). Small bulges like the Milky Way’s may have formed by secular processes involving central bars (Pfenniger & Norman 1990; Courteau et al. 1996), tying the evolution of the bulge to the disk. M31’s bulge is too large to have formed by this

mechanism.

The question of the difference between a large $R^{1/4}$ bulge with moderate rotational support and a non-rotating halo is not just one of taxonomy: the formation processes of these two populations are quite different. A kinematically hot, non-rotating stellar halo is most simply formed **after** the aggregation of the galaxy’s dark halo — this explains the lack of correlation between the angular momenta of the halo and the disk (Freeman 1996). This scenario is supported by growing evidence that the Milky Way halo was populated, at least in part, by the accretion and destruction of small satellites (Majewski, Munn, & Hawley 1994; Helmi et al. 1999; Ivezić et al. 2000; Yanny et al. 2000; Dohm-Palmer et al. 2001). The Sgr dwarf (Ibata, Gilmore, & Irwin 1994) and its tidal streams give a present-day example of this process.

But the accretion history of the Milky Way may be dramatically different from that of a galaxy of earlier Hubble type like M31. An $R^{1/4}$ profile is a result of violent relaxation such as occurs, for example, in major mergers. We note that both accretion and merging involve interaction between galaxies, but the mass ratios are very different: in the merger which forms an $R^{1/4}$ law profile, the mass ratio is at most a few to one, while the mass ratio for the accretion of small satellites to form a hot halo is more typically 100:1 or more. As a result, major mergers have a strong effect on the galaxy disk while the accretions have almost none.

Does M31 actually have a kinematically hot halo? If so, how much luminosity does it contribute? Accurate kinematic data for halo objects are needed to **quantify** the relative importance of this process in populating the outer regions of M31. However, the difficulty in isolating the halo from the bulge and in obtaining accurate velocities for halo populations has precluded a definitive answer to these questions. Spectroscopy of single field stars in M31 is very challenging, even for giant-branch tip stars using Keck, as samples are dominated by contamination by foreground stars from the Milky Way (Reitzel, Guhathakurta, & Gould 1998; Reitzel & Guhathakurta 2002).

Globular clusters have been the halo tracer of choice thus far, but present several difficulties. Cluster velocities derive from absorption spectra, and accurate velocities (errors < 20 km/s) are only now becoming available (Perrett et al. 2002; P. Seitzer 2002, private communication). Thus, early studies of M31 cluster kinematics concluded that its halo had little rotation (Huchra, Brodie, & Kent 1991; Huchra 1993), while more recent studies find greater rotational support (Perrett et al. 2002). In the Milky Way, the field stars and globular clusters share a similar metallicity distribution (Zinn 1985; Laird et al. 1988; Ryan & Norris 1991) and "hot" kinematics (Norris 1986; Beers et al. 2000). However, in M31, the abundance distribution of the clusters and the field stars at similar radii are quite differ-

ent; the clusters are more metal-poor in the mean than the field stars (Durrell et al. 2001; Barmby et al. 2000). Because cluster metallicities differ, cluster kinematics also may not be entirely representative of the stellar halo properties.

Planetary nebulae (PN), in contrast, trace stellar populations with ages $\sim 1\text{--}10$ Gyr and readily give accurate velocities with 4m-class telescopes, because almost all their energy output is concentrated in a few emission lines. The techniques for detecting PN have been well-documented by G. Jacoby and collaborators (Jacoby et al. 1989). PN have been used extensively as kinematic tracers in normal ellipticals (Hui et al. 1995; Arnaboldi et al. 1996; Méndez et al. 2001), and in the luminous members of the Local Group (Nolthenius & Ford 1986, 1987). Nolthenius & Ford (1987, hereafter NF87) presented kinematics of 37 M31 planetary nebulae, with distances along the major axis of up to 40 kpc and distances from the major axis of up to 17 kpc. Although it is possible to identify the signatures of disk and bulge in their data and find a few objects with clear halo kinematics, the small size of their sample precludes strong conclusions.

Here we present the results of a kinematic survey of 135 PN in one quadrant of M31’s outer bulge/halo. The survey extends to 20 kpc along the minor axis, well into the canonical halo regions of M31, and 20 kpc along the southwest major axis. We have used both the spatial and kinematic information for the PN to distinguish the bulge population from the halo population. With this larger number of PN and the accurate velocities (errors of 5–10 km/s) resulting from the follow-up Hydra spectroscopy, we have a clearer picture of M31’s spheroid. Using the Milky Way as a guide, we expected to find only a small degree of rotational support in the populations far from the major axis, similar to the Milky Way’s stellar halo. Instead, we find that the bulge dominates out to the limits of our survey, and that very few objects belong to a non-rotating, pressure-supported halo like the Milky Way’s.

In Section 2 we describe the survey which identified our PNe and the spectroscopic follow-up to obtain velocities. In Section 3 we present the PN kinematics and discuss the spatial and kinematic signatures of the thin disk, halo and bulge in M31 with relation to these results, concluding that a thin disk and a dominant bulge best explain our data. In Section 4, we interpret the kinematics in the context of formation scenarios for these populations.

2. Observations

2.1. PN Detection and Photometry

Our PN detection relies on the fact that PN have a very strong OIII emission line at $\lambda 5007$ and relatively little continuum emission. Distant PN can therefore be detected via

narrow-band imaging at $\lambda 5007$. Exposures at a nearby but offset wavelength can be used to discriminate PN from stars.

Imaging of M31 was carried out at the CWRU Burrell Schmidt on the nights of 23-30 September 2000. The camera at the Schmidt has a SITe $2K \times 4K$ back-illuminated CCD with 15 micron pixels and a pixel scale of $\sim 1.45''/\text{pixel}$. It covers a $40'(\text{E-W}) \times 80'(\text{N-S})$ field. The readnoise during the Schmidt imaging run was $12e^-$ and the gain was $1.8e^-/\text{ADU}$. The seeing ($2\text{--}2.5''$) was typical for the Schmidt.

The choice of filter depends on several factors, and some issues regarding filters are discussed in Jacoby et al. (1992). The [OIII] $\lambda 5007$ filter should be narrow enough to minimize the sky contribution, yet wide enough to accommodate the potentially large range of velocities. It should also be well-matched to the observed wavelength of the [OIII] $\lambda 5007$ emission line. M31's systemic velocity is -300 km/s (de Vaucouleurs et al. 1991), so that the [OIII] $\lambda 5007$ line is shifted blueward to 5002\AA . A blueward shift of 13\AA in the filter response results from the Burrell Schmidt's $f/3.5$ beam (this accounts for a shift of $\sim 10\text{\AA}$), and the temperature difference between the lab where the filter response curve published by NOAO was measured and the observing conditions ($\sim 3\text{\AA}$). For Fields 1 and 2, we used filter KP1590 with $\lambda_c = 5022\text{\AA}$ and for Field 3, filter KP1467 with $\lambda_c = 5008\text{\AA}$.

The filter transmission for a velocity of ± 400 km/s with respect to M31's systemic velocity (the likely worst case) is $\gtrsim 70\%$ in all cases (Figure 1). We note that the filter used for Field 3 has a 15% gradient across the velocities of interest. Detection of disk PN is unaffected, as the field is located on the approaching side of the galaxy and the emission is blueshifted into the higher sensitivity region of the transmission curve. Also, the gradient across disk velocities will be negligible due to the relatively low dispersion of disk PN (< 100 km/s). Detection of halo objects may have been slightly biased against those with velocities more than 200 km/s greater than the systemic velocity in that field. Although we have not quantified this effect, it would not alter our final conclusions.

We placed our fields to sample halo PN and to measure their rotation. Fields 1 and 2 lie along the minor axis of M31, and Field 3 covers a region at larger radius which includes the major axis. Figure 2 shows their placement on an image of M31 kindly provided by Rene Waltherbos. Field 1 was observed under photometric conditions; Fields 2 and 3 were observed during periods of thin cirrus and occasional heavy cloud. Fortunately, these observations are still usable because the focus of this project is the PN velocities rather than the photometry. We followed standard image reduction procedures. The images were bias-subtracted and flatfielded, and then registered using bright stars in the field. We averaged them using

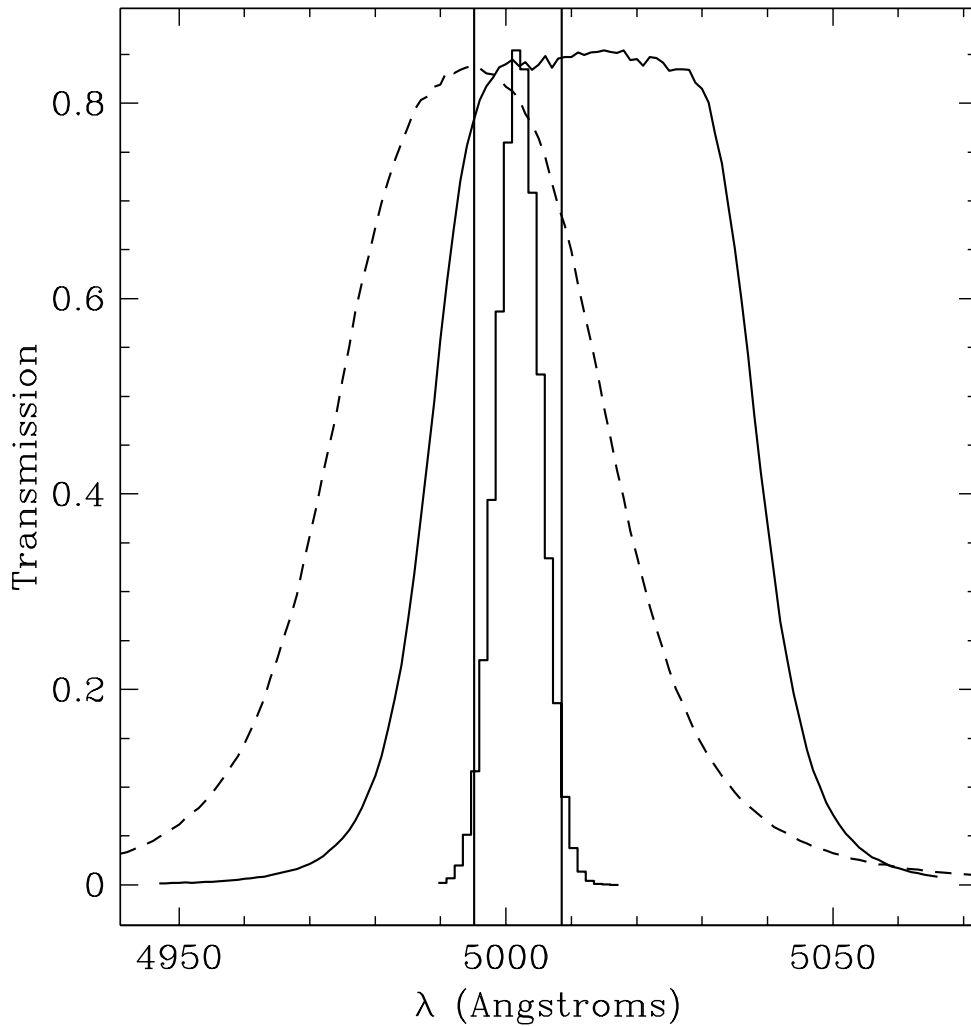


Fig. 1.— Filter transmission curves for this survey. Solid line: curve for KP1590, used for Fields 1 and 2. Dashed line: curve for KP1467, used for Field 3. Both curves have been shifted 13 Å blueward to account for the f/3.5 beam of the Schmidt and the observing temperature. The histogram is a Gaussian distribution with mean -300 and $\sigma = 200$ km/s representing the expected M31 halo velocity distribution. The vertical lines show the location of velocities ± 400 km/s from M31's systemic velocity.

IRAF¹ *imcombine* with *ccdclip* rejection.

Because we were primarily interested in the kinematics of the halo and populations, we wanted to exclude HII regions from our sample as much as possible, as they belong to the young, thin disk. The geometry discussed in Section 3.1.1 shows that HII regions confined to the disk should be rare more than about 3 kpc from the major axis. Therefore, we limited our selection of PN from the Schmidt data to those more than 3 kpc from the major axis near the center of the galaxy. At larger radius, where the background light from the disk was fainter, it was easier to distinguish point-like PN from more extended HII regions and we allowed the sample to extend to the major axis. Jacoby, Ford & Hui kindly shared positions for some of the objects from their earlier survey of the M31 disk and bulge (Hui, Ford, & Jacoby 1994). During the follow-up spectroscopy run, we assigned spare fibers to these objects, some of which are nearer the center than the Schmidt sample.

To identify PN candidates, we generally followed the procedure outlined by other PN studies such as Ciardullo et al. (1989). For our project, however, it was not possible to perform photometry on a difference of the on-band image and the appropriately scaled off-band image. This is because the PSF varies across the field of view of the Schmidt – due to the curved focal plane – and depends sensitively on the seeing and focus. Large residuals on the difference image would lead to many false detections. Instead, we used DoPHOT (Schechter, Mateo, & Saha 1993) on the combined on- and off-band images separately and matched the resulting object lists. We then matched the position of objects in the on-band image with objects in the off-band image within a 2 pixel radius. Objects in the on-band image which had no counterpart in the off-band object list were classified as PN candidates.

All candidates were visually verified. To be included in our list of spectroscopic targets, a point-source in the on-band image should have no discernible flux at the same position in the off band image. Faint candidates were also required to have at least some signal present in each of the four exposures taken under the most transparent conditions. We ranked the PN candidates by the degree to which they satisfied all the criteria. As we will discuss below, $\sim 88\%$ of our first priority PN candidates were confirmed spectroscopically, validating our selection criteria. Figure 3 shows the PN luminosity functions for confirmed PN in Fields 1 and 3. The rough calibration is based only on assigning the brightest PN to $M_{5007} = -4.5$ (Ciardullo et al. 1989). We reached basically to equal depths of 1.5–2 magnitudes down the PN luminosity function in these two fields. There were only 5 objects in Field 2, and their

¹IRAF is distributed by the National Optical Astronomy Observatories, which is operated by the Association of Universities for Research in Astronomy, Inc. (AURA) under cooperative agreement with the National Science Foundation.

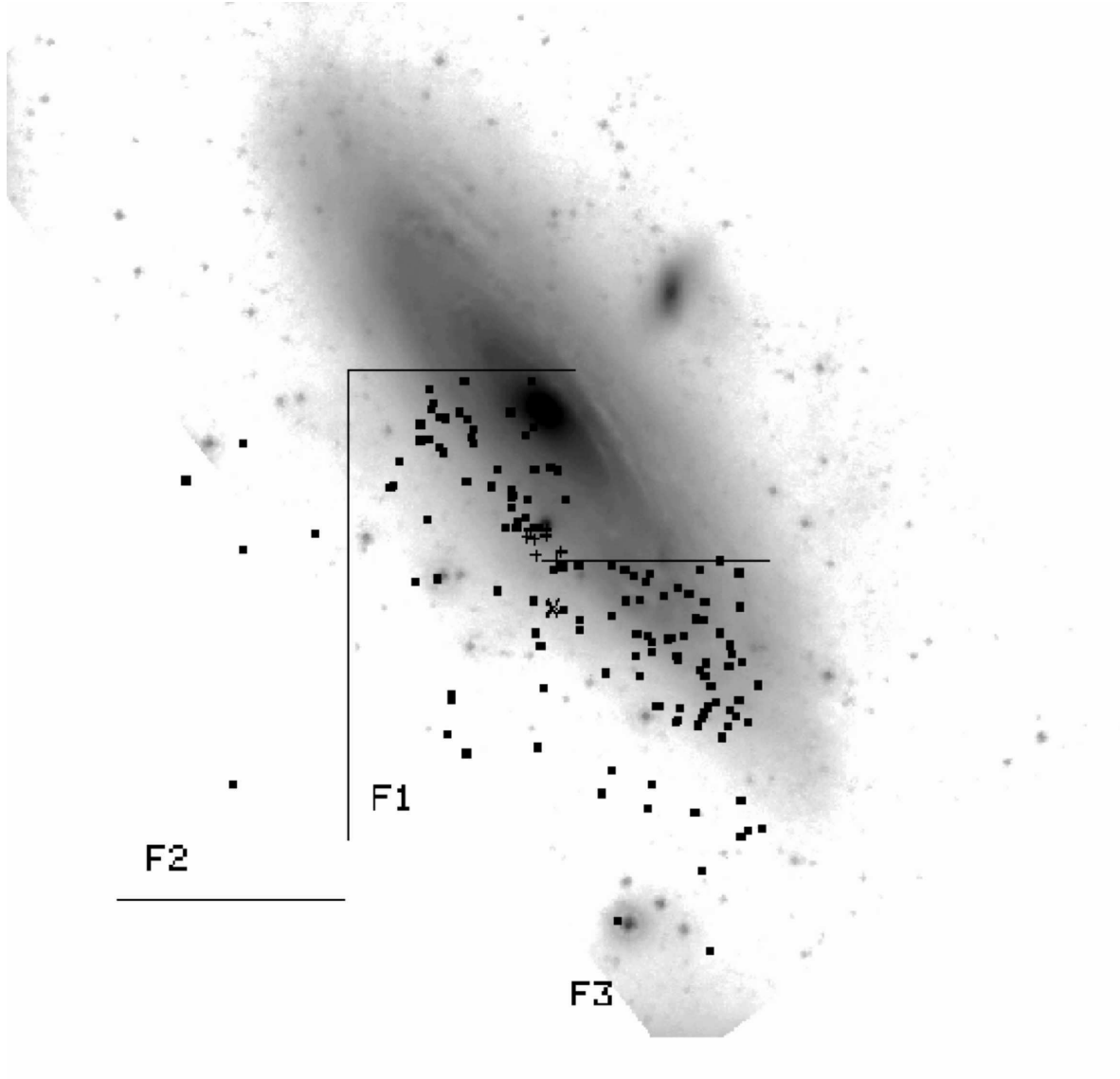


Fig. 2.— Positions of our Schmidt fields and PN in M31. The R-band image was kindly provided by Rene Walterbos. North is up, East is left. M31’s position angle is 37.3° (de Vaucouleurs 1958). The SW end of the galaxy is approaching, and the far side is to the SE of the major axis. Squares: PN in M31. Pluses: PN in M32. Xs: HII regions in And IV.

photometry is consistent with the other two fields.

2.2. Astrometry

The WIYN² Hydra fiber spectroscopy of these candidates requires positions accurate to better than 1". We identified astrometric standards from the USNO-A 2.0 astrometric catalog (Monet et al. 1998) in each of our three fields. From these reference stars, we computed the transformation between the DoPHOT coordinates and the celestial coordinate system using the *tfinder* and *ccmap* packages in IRAF. With $\gtrsim 1000$ reference stars in each field and the high accuracy of the catalog positions, an accurate transformation was possible even over the large field of the Schmidt. The rms error in the calculated positions was less than 0.3" in all fields.

2.3. Spectroscopy

The spectroscopic observations were obtained with the WIYN Hydra fiber spectrograph on the night of 7 September 2001. The conditions were clear with good seeing, and we were able to obtain spectra for all of our candidates. For the instrument configuration, we used the red fiber set with the 600 lines/mm grating in first order. This provided a wavelength range from 4800 to 6800 Å, a dispersion of 1.4 Å per pixel, and a resolution of 2.9 Å.

The three Schmidt fields were divided into 6 separate Hydra fiber setups. For each setup, we took a series of four 600s exposures and a Copper-Argon (Cu-Ar) lamp exposure. At the beginning of the night, we took a series of dome lamp flatfield exposures at a neutral position. More accurate flatfielding was unnecessary, as the PN in our sample are relatively bright and we are only interested in velocities. The spectra were overscan subtracted, trimmed and bias subtracted via standard IRAF routines. The individual fiber spectra were extracted using the fiber apertures determined from the dome flats. We then coadded spectra from the individual exposures to make the single deep spectrum for each object.

Highly accurate velocities depend upon careful wavelength calibration of the spectra. We used the adjacent Cu-Ar lamp exposure for each setup to wavelength calibrate the individual spectra. A fifth order Legendre function was used to fit 60–70 lines in the Cu-Ar spectrum to determine the spectral solution. The rms error in the fits was always less than 0.2 Å, or

²The WIYN Observatory is a joint facility of the University of Wisconsin-Madison, Indiana University, Yale University, and the National Optical Astronomy Observatory.

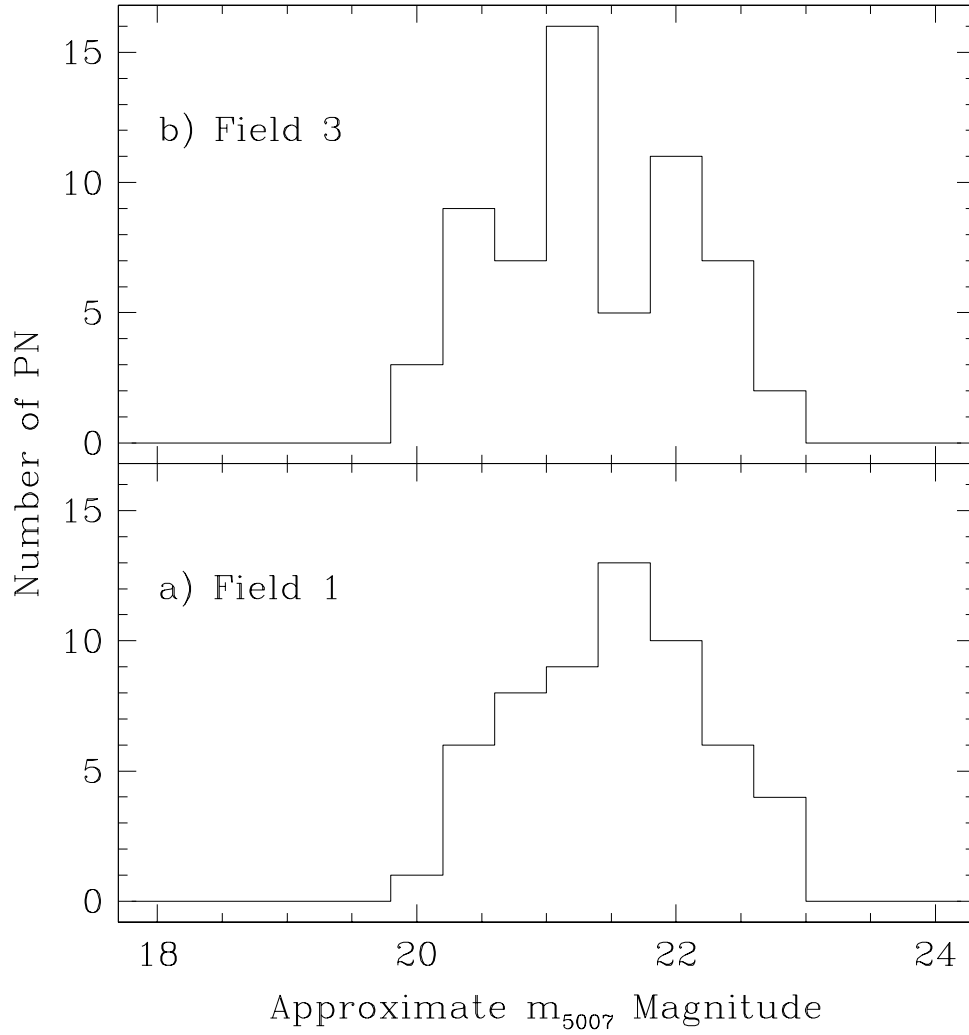


Fig. 3.— The estimated PN luminosity function for Fields 1 (panel a) and 3 (panel b). The X axis is the instrumental [OIII] $\lambda 5007$ distribution shifted so that the bright edge of the distribution is at $m_{5007} = -4.5$.

10 km/s. The bench-mounted spectrograph minimizes the spectral shift. We confirmed this by cross-correlating the comparison lamp spectra from different pointings, and found that the spectra shifted by less than 0.05 \AA over the course of the night. Figure 4 shows three typical spectra from our sample.

Unlike studies of PN kinematics in distant galaxies where only [OIII] $\lambda 5007$ is detected (e.g. Hui et al. 1995; Arnaboldi et al. 1998; Méndez et al. 2001), the proximity of M31 PN allows us to easily detect $\lambda 5007$ and $\lambda 4959$ in nearly all of our candidates, and $H\beta$ in most. Local Group PN studies which have used all three lines *independently* (e.g. Nolthenius & Ford 1987; Ford, Jacoby, & Jenner 1977) have found that they lead to systematically different velocities. We opt instead to use all three lines simultaneously, thus improving the accuracy of our derived radial velocities.

We used the *rv* package in IRAF to derive radial velocities using the cross-correlation of the object spectra with a template. Initially we created an artificial PN spectrum to serve as the template spectrum (three lines matched to the instrumental PSF at $\lambda 5007$, $\lambda 4959$, and $H\beta$), but found that we were able to reduce the internal velocity errors significantly by using a spectrum created by combining real PN spectra as a template. We selected the 8 highest signal-to-noise spectra from the PN in the first pointing. After continuum-subtracting them, we shifted them to zero velocity by fitting a Gaussian to the $\lambda 5007$ line profile. The final template was created by coadding these 8 spectra. The radial velocities are derived by calculating the cross-correlation function of the template and continuum-subtracted PN spectra in the spectral region including $\lambda 5007$, $\lambda 4959$, and $H\beta$, using *fxcor* in IRAF. In general, we did not sky subtract the PN spectra as there were no significant sky lines or stellar absorption lines in this spectral region. The resulting radial velocities and errors are listed in Table 1.

2.4. Velocity Errors

All the PN were observed on the same night with the same instrument, making systematic differences within the PN sample highly unlikely. We observed 11 PN from our sample in multiple pointings. The mean difference in velocity for these PN is -1.2 km/s with a standard deviation of 4 km/s . These results are consistent with the typical internal velocity error estimates from *fxcor* of $3\text{--}7 \text{ km/s}$. We estimate an additional 5 km/s of error in the velocities due to systematics effects.

There have been several earlier studies of emission-line objects in or near M31, and this allows us to assess the systematic error in our velocities. We have spectra for three HII

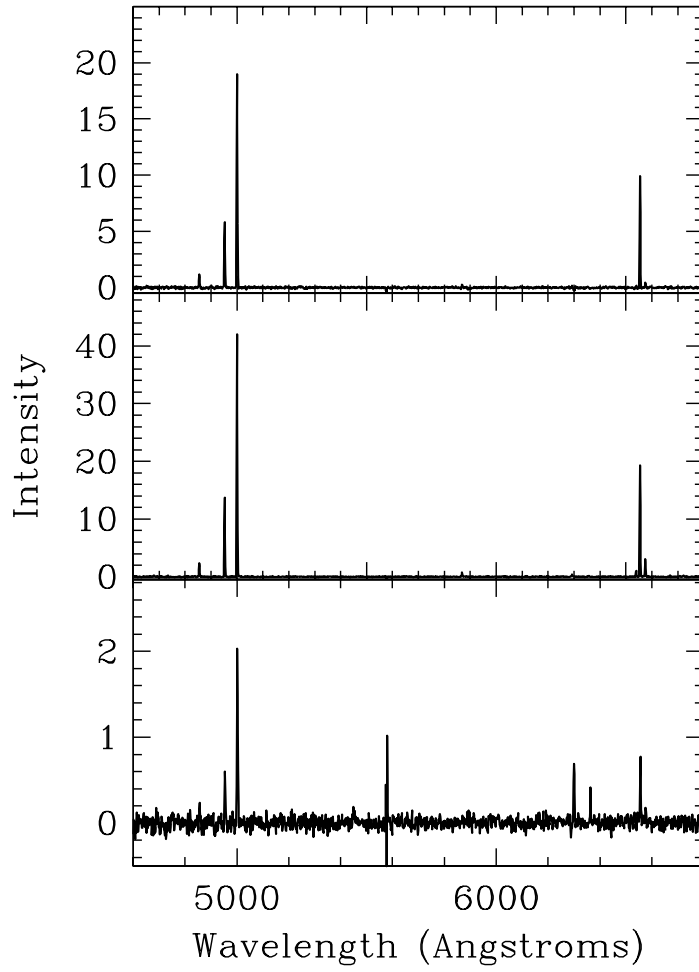


Fig. 4.— Three typical spectra for our sample, with a range of signal-to-noise, showing the strongest PN emission lines, [OIII] λ 4959 and λ 5007, and H α .

regions in the dwarf galaxy And IV (objects 3, 4 and 6 from Ferguson, Gallagher, & Wyse 2000). The velocities for objects 4 and 6 agree within 5 km/s (250 ± 5.2 and 270.8 ± 39.2 , respectively compared to 250 and 273 km/s from Ferguson et al. (2000)). For object 3, we find a velocity of 233.0 ± 3.4 km/s compared to 244 km/s, a difference of 11 km/s. Our sample and that of NF have 11 PN in common. The mean difference $v_{thispaper} - v_{nothenius87}$ is 10.4 km/s. This is the same systematic difference that NF87 note between their velocities and those of Ford et al. (1977) for the Galactic PN velocity standards used in the two studies. Given the good agreement between our velocities and those of Ferguson et al. (2000), and the disagreement between the NF87 and Ford et al. (1977) velocities, we conclude that there is a systematic offset in the NF87 velocities. In the remaining discussion, we have offset their velocities by +10.4 km/s to agree with ours.

3. Results

3.1. Overview of PN Kinematics

Although M31 is the primary target of our survey, M32 and the dwarf galaxy And IV are also located in the survey region. Membership for several objects is ambiguous and was decided based on position and velocity.

The three emission line objects we identified in And IV are HII regions, resolved in HST images (Ferguson et al. 2000). Although PN commonly have $\xi = [\text{OIII}]\lambda 5007/\text{H}\alpha \sim 3$, values nearer to 1 are possible, so that ξ for PN and high-excitation HII regions overlap significantly. This ambiguity prevents distinguishing PN from HII regions solely with our spectra; such a distinction requires nebular modelling which relies on faint lines beyond our wavelength range. The inclusion of the And IV HII regions in our sample raises the question of substantial numbers of M31 HII regions in the sample. However, this is unlikely for several reasons. The And IV HII region spectra have $\xi \sim 1/3$, much less than the rest of our sample. And IV is significantly more distant than M31 (>5 Mpc; Ferguson et al. 2000). Bright M31 HII regions are more likely to be resolved, and we considered only point sources as candidates. Also, though the value of ξ ranged from 1–3 (excluding the And IV HII regions), objects with values as low as 1 are rare in our sample ($<10\%$). With this in mind, we refer to the emission line objects in M31 as PN throughout the rest of the discussion.

M32 PN are clumped in position and in velocity near M32’s radial velocity of -197 km/s (Huchra et al. 1999). For M32, $\sigma_v \sim 50$ km/s and the tidal radius is ~ 2 kpc (Mateo 1998). Nine PN in the sample have velocities within 50 km/s of M32’s systemic velocity and are located within 1 kpc of M32’s center. PN membership is summarized in Tables 1, 2 and 3.

Each table lists the positions and heliocentric radial velocities for the emission line objects in M31, M32 and And IV, respectively. We have excluded M32 and And IV objects from the analysis that follows.

The positions of the PN relative to the center of M31 are shown in Figure 5. We have assumed a distance of 770 kpc to M31 (Freedman & Madore 1990). X is distance in the major axis direction, and Y is the distance in the minor axis direction. The positions have been rotated through M31’s position angle (37.3° de Vaucouleurs 1958) so that the major axis defines $Y = 0$. All velocities are plotted relative to M31’s systemic velocity and coded by symbol size. We have enlarged our sample of PN by adding the objects from NF87 which are not already in our sample.

The depth and spatial sampling of the survey is not uniform and must be taken into account when interpreting the spatial distribution of the PN. Only Field 3 intersects the major axis (compare Figure 2 and Figure 5). Fields 1 and 2 had a sizable gap between them and this can be seen in Figure 5 around $Y = -12$ kpc. Fields 1 and 3 are of comparable depth, while Field 2 is shallower. Finally, the objects nearest the center of the galaxy, where we did not attempt to identify PN in the Schmidt images, are PN from the sample of Hui, Ford, & Jacoby (1994) used to fill spare fibers, as mentioned previously.

The various populations in M31 can be isolated by splitting the sample in Y . Figure 6 shows plots of distance along the major axis vs. the line-of-sight velocity for several ranges of $|Y|$. The disk dominates at $|Y| < 0.5$ kpc, where the upper limit on the PN velocities is the HI rotation curve (Kent 1989). A mixture of disk and bulge objects are seen at $|Y| = 0.5 - 6$ kpc. Bulge PN near the minor axis of the galaxy have velocities of -150 to 150 km/s relative to M31’s systemic velocity, consistent with the large bulge central velocity dispersion of $100-150$ km/s (McElroy 1983; Richstone & Shectman 1980). Some of the highest velocity objects in this region (crosses) may be associated with the newly discovered satellite And VIII (Morrison et al. 2003b). We expect to find bulge and halo objects at $|Y| > 6$ kpc. We discuss the distinction between these regions further in Section 3.2.

A striking feature of Figure 6 is the very small number of PN occupying the “forbidden” quadrants for disk objects, even at large Y . This lack of objects in the two non-disk quadrants is the signature of a rotationally supported population, which clearly dominates our sample.

Disentangling the various stellar populations in M31 is complicated by the galaxy’s inclination (77° from face-on) which causes objects in the outer disk to appear in projection away from the major axis. Disk, bulge and halo populations therefore overlap spatially and kinematically. The combination of position and velocity data, however, offers the potential to isolate the different populations. The allowed velocities for a given PN position will depend

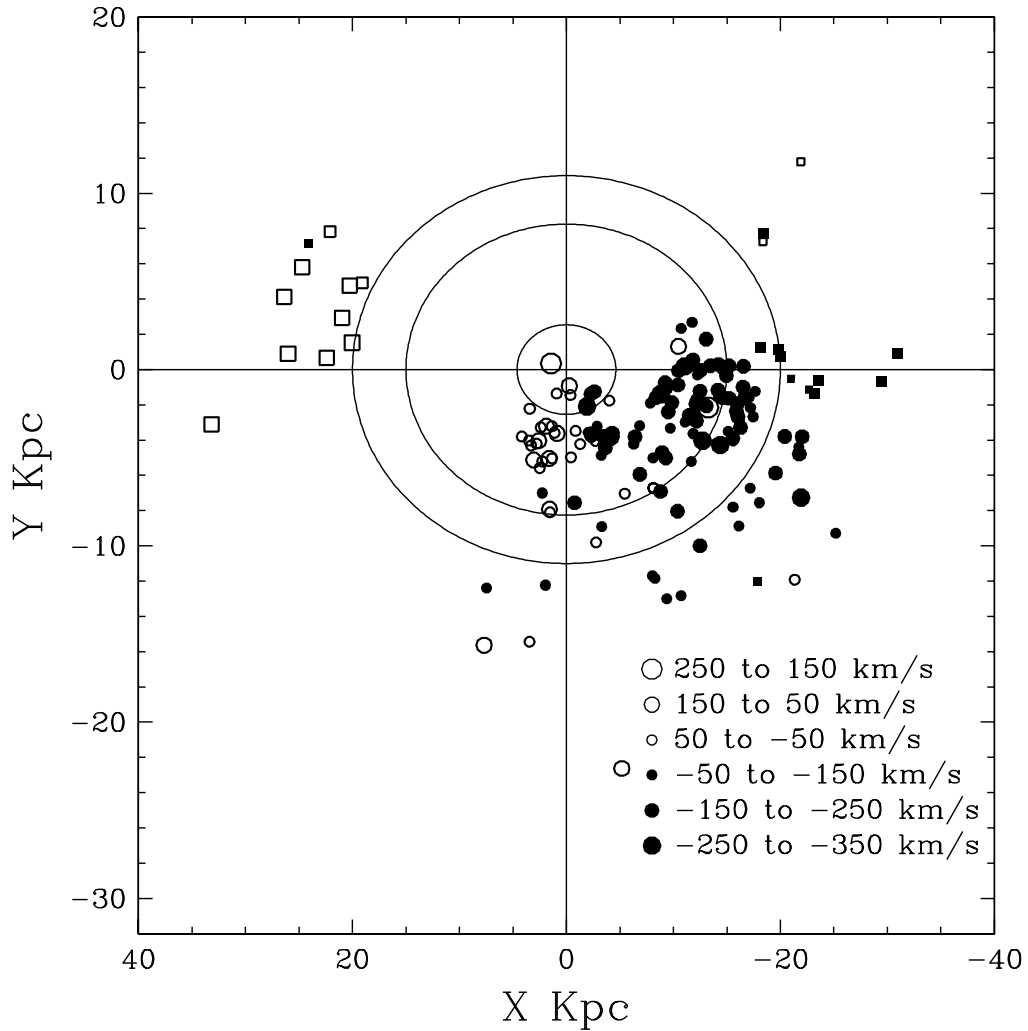


Fig. 5.— Plot showing the positions of PN in M31. The major axis has been rotated through the position angle so that it is horizontal in the figure. Symbol size corresponds to velocity. Circles are PN velocities from this study, and squares are those from NF87. Ellipses are bulge isophotes with $b/a=0.55$.

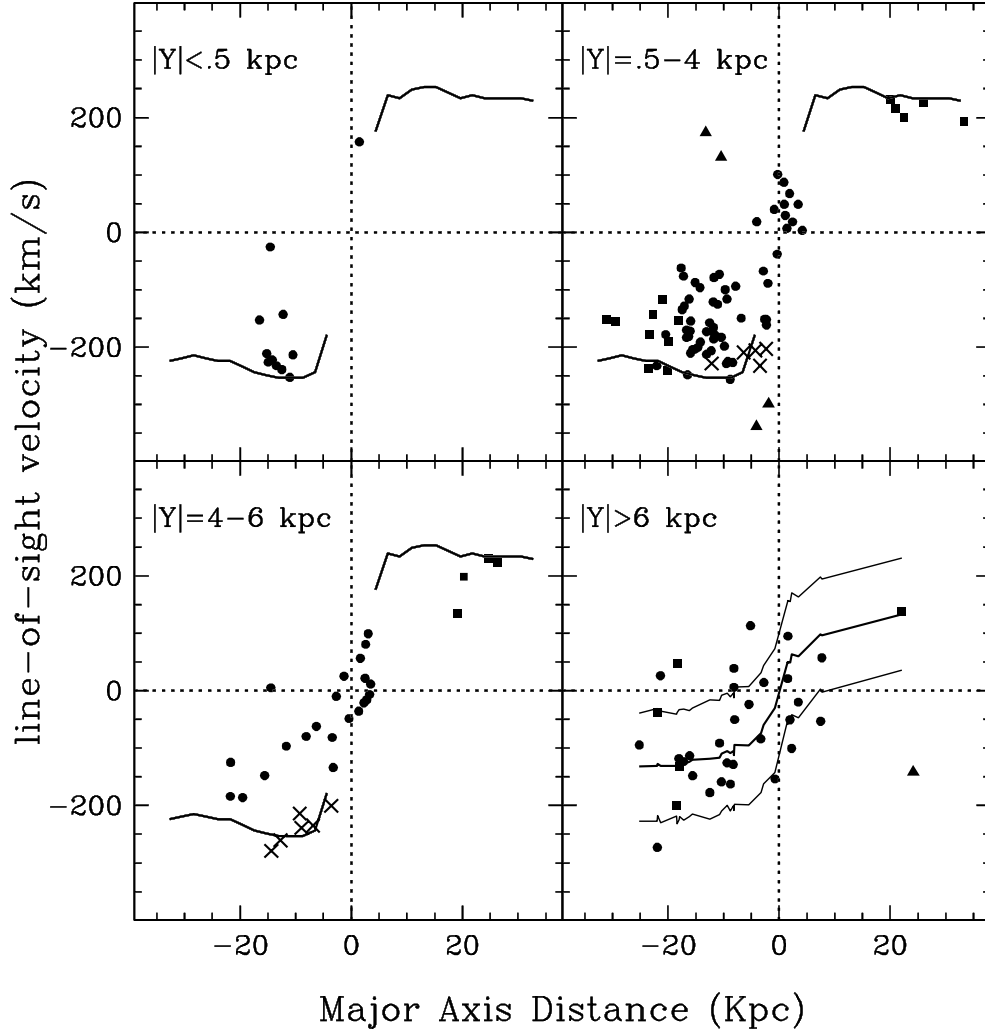


Fig. 6.— Velocity-distance diagram for PN in M31. X is distance along major axis; Y is the projected distance in the direction of the minor axis. Colors for the electronic edition are listed in parenthesis: Filled circles (PN from our survey) and squares (PN from NF87) are PN with M31 disk or bulge velocities (black); triangles are halo candidates (red); crosses are probable And VIII members (Morrison et al. 2003b) (blue). The rotation curve is taken from Kent (1989). The solid lines in the lower right panel represent the range of values which could be expected for the PN for our best bulge model as discussed in section 3.4.

on the kinematic population to which it belongs. In the discussion that follows, we present an overview of the expected spatial and kinematic signatures of the disk and bulge, then use simple kinematic models to distinguish between them, as well as identify halo candidates. We adopt the following definitions: v_{los} and σ_{los} are the observed, line-of-sight velocity and dispersion, respectively; for a given population, v_{rot} is the rotation velocity and σ_r is the radial velocity dispersion; v_{circ} is the circular velocity of the disk, which reflects the mass distribution, and which we take to be the HI v_{rot} , roughly 250 km/s.

3.2. M31’s Inclined Disk

3.2.1. Spatial Extent of the Disk

The spatial signature of the disk will depend on the size and thickness of the disk, as well as the degree of warping and the radius at which the warp begins. However, we can draw some simple conclusions from basic geometry. The radial extent of the optical stellar disk was estimated by WK88 to be 26 kpc. There are now two very deep star count images that can be used to check this result, from Ferguson et al. (2002) and Zucker et al. (2004). These images reach to of order 30 V mag/arcsec², and are thus very sensitive tests for the extent of the disk. In both images it can be seen that the brighter portions of the outer disk extend to the WK88 value, there are some fainter regions which extend to R=35 kpc and may be associated with tidal streams or with the outer disk, and that there is no starlight beyond 35 kpc to very sensitive limits. We have thus assumed R_{max} =26 kpc and consider the effect of a larger R_{max} when relevant in the discussion that follows.

If the disk were planar and non-warped, its edge would project to a distance of 5.6 kpc from the major axis because of M31’s inclination. Near the minor axis, the disk and bulge contribute roughly equally to the luminosity from 2–5 kpc (see Figure 3 of WK88). We can therefore expect the bulge and halo PN to dominate beyond \sim 5 kpc from the major axis. These rough geometrical arguments are supported by observations. On the side of the major axis covered by our survey, the outer optical isophotes of the galaxy ($\mu_B \sim 26$) extend 4.4 to 6.6 kpc (20–30 arcmin) from the major axis (WK88); HII regions are found up to 4 kpc (Pellet et al. 1978).

However, the assumption of a perfectly planar disk is not justified. Neutral hydrogen studies (Roberts & Whitehurst 1975; Cram, Roberts, & Whitehurst 1980; Brinks & Shane 1984) have found two distinct velocity systems for many lines of sight through M31’s disk. This suggests that the line of sight is crossing the disk twice. Brinks & Burton (1984) interpreted the dual kinematics as a warp signature. In their model, the geometry of the

galaxy is such that the line of nodes is nearly aligned with the major axis and the warp bends over back toward the major axis on the near (NW) side, so that the warp is nearly edge-on (Brinks & Burton 1984, Figure 2a). The unwarped HI has a radius of 16 kpc, which would project to a height of 4 kpc from the major axis.

Brinks & Burton (1984) introduce a flare of increasing scale height in their model of the HI warp. The flare crosses the line of sight to the major axis and accounts for the two velocity systems there. Flares are common in the outer HI disks of galaxies (Sancisi & Allen 1979; Kulkarni et al. 1982; Olling 1996), but the evidence for flared **stellar** disks is conflicting. Studies of other galaxies have generally found a constant stellar scale height at all radii (van der Kruit & Searle 1981; Morrison, Boroson, & Harding 1994). Recent in situ analyses of Milky Way stars, however, suggest that its stellar disk may be flared (Lopez-Corredoira et al. 2002; Drimmel & Spergel 2003). Drimmel & Spergel (2003) find that a flare parameter of 6.6 pc/kpc slightly improves their model fits. However, this amounts to an increase of less than 0.25 kpc over the entire length of the disk. This is a relatively small increase, and would be indistinguishable from an unflared disk in our data.

Braun (1991) analyzed existing HI data and concluded that the warp model is too simple. He suggested that the data were better explained by a more complex change in position of the HI disk’s midplane, perhaps caused by gravitational perturbations from M32. In this model, the position of the disk midplane varies from 500 pc above the nominal plane to 1 kpc below it (see Braun 1991, Figure 10). If M31’s disk had been disturbed by M32’s passage, dynamical evolution may have thickened the stellar disk to an even larger scale height. However, the cold disk kinematics of some globular clusters rules out a major interaction, making a disk thickened in this way unlikely (Morrison et al. 2003a). Based on these arguments, we expect that the disk’s luminous influence should have waned entirely by $Y = 5 - 6$ kpc.

3.2.2. *Kinematic Signature of the Disk*

The disk’s distinctive kinematic signature can be illustrated by first considering a simple edge-on disk with zero velocity dispersion and constant circular velocity; a schematic is shown in Figure 7. The line of sight through a given major axis distance, X , intersects the disk at different radii resulting in different projections of the rotation velocity, v_{rot} , into the line of sight. At a single value of X , any velocity between that at A and that at C is allowed. The lowest velocity allowed decreases towards the center of the disk where the line-of-sight velocity, v_{los} , is zero. Corresponding simulated velocity-distance diagrams are shown in Figure 8. Disk objects will be found in only two of the four quadrants of the

velocity-distance diagram, corresponding to the approaching and receding sides of the disk.

Because the disk is inclined rather than exactly edge-on, distance Y from the major axis correlates with position in the disk. For example, lines of sight through the major axis intersect the orbital tangent point (left panel); v_{los} is the component of v_{rot} projected into the line of sight through the inclination. Lines of sight through the disk between B and C (right panel) exclude the major axis points and can have only lower values down to the lowest allowed by the edge of the disk. This basic geometry also holds for a more realistic, hotter disk with some velocity dispersion, although the velocity dispersion tends to smooth out sharp features.

3.3. Disk PN Kinematics

PN near the major axis are those most likely to be disk objects (Figure 6, upper left panel). There are 10 PN with $|Y| < 0.5$ and $|X| > 10$. One object near $X = -13$ kpc has $v_{los} = -25$ km/s, more than 200 km/s from the HI rotation velocity, and probably belongs to the bulge or halo, so we have excluded it from the disk sample. The 9 remaining PN have an average v_{los} of 215 km/s with $\sigma_{los} = 39$ km/s.³ σ_{los} is dominated by the σ_ϕ component of the velocity ellipsoid on the major axis, implying $\sigma_r \sim 55$ km/s.

However, these values of v_{rot} and σ_r are very uncertain. First, the inclusion of off-axis PN in the average systematically reduces the measured mean v_{los} . Second, the sample is very small, and the statistics do not take into account the possible inclusion of bulge PN. At this distance along the major axis, the bulge contributes $\sim 15\%$ of the total luminosity (WK88), or potentially 1–2 PN of the 9 in this sample. Two PN have velocities more than 100 km/s from the HI rotation and removing those increases the average v_{rot} to 234 km/s, and reduces σ_r to 20 km/s. Third, the disk rotation velocity is not a secure measurement and is uncertain at the 10-20 km/s level; see the discussion in Morrison et al. (2003a).

With this sample, we cannot distinguish between a thin and thick disk, and more disk PN are needed (Merrett et al. 2003, D. Hurley-Keller et al., in preparation). Morrison et al. (2003a) show that a large subsample of globular clusters which project on to the disk have thin disk kinematics. This suggests there has been no merger with M31 large enough to disrupt its thin disk since the formation of the clusters and is compelling evidence against a thick disk in M31.

³These values have been corrected for M31’s inclination. We have dropped the negative sign indicating rotation toward the observer throughout the remainder of the paper.

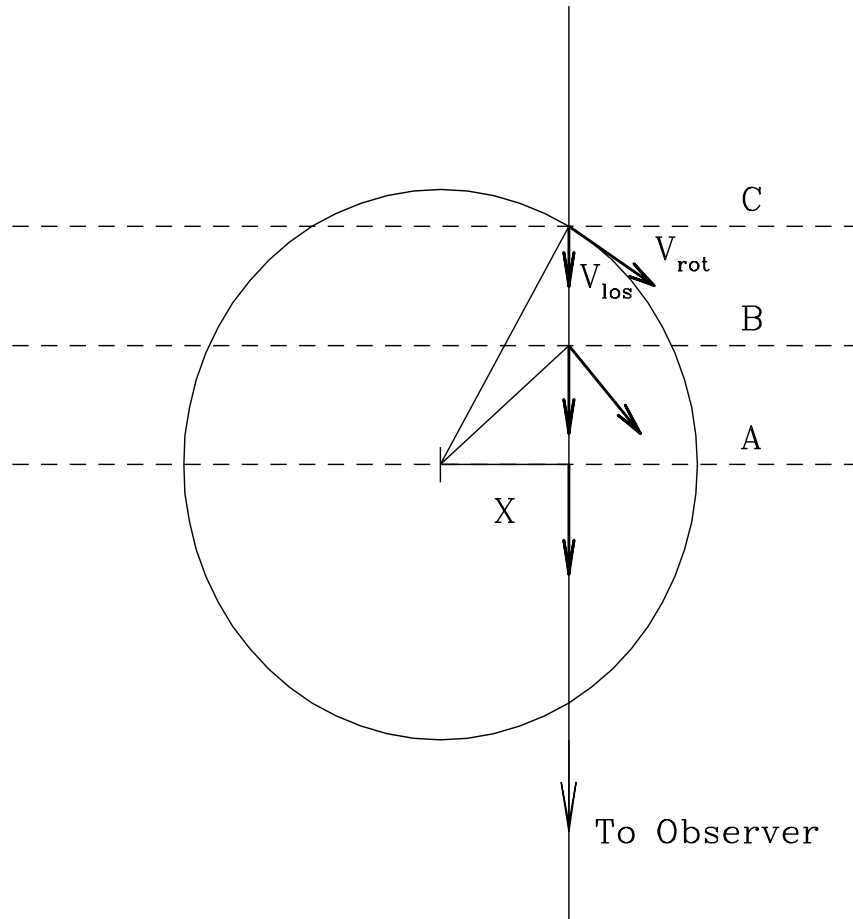


Fig. 7.— Schematic of an edge-on disk, viewed from above. The observer is off to the bottom. v_{rot} is the rotation velocity, and v_{los} is the observed radial velocity. The major axis as observed would lie along line A. The tangent point occurs at A where $v_{los} = v_{rot}$.

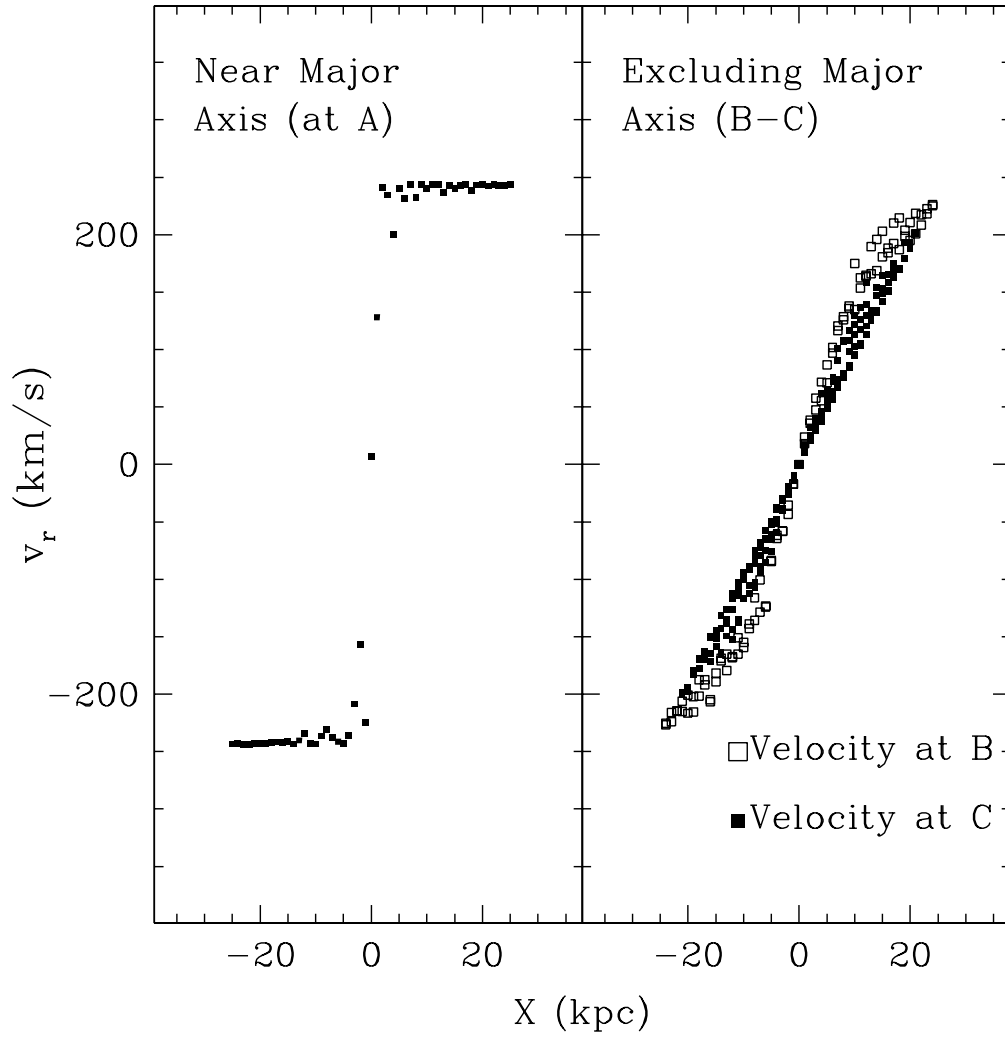


Fig. 8.— Velocities from a model disk, as in Figure 7, but with M31's v_{circ} and inclination.

3.4. Beyond the Disk: Bulge and Halo

At $|Y| > 6$ kpc, the PN kinematics are still dominated by rotation (Figure 6, lower right panel). The mean v_{los} of the PN with $|X| > 10$ and $|Y| > 6$ is 116 km/s, with $\sigma_{los} = 79$ km/s. These PN clearly do not belong to a high velocity dispersion, non-rotating halo like that of the Milky Way. To what population do they belong?

3.4.1. Overview of Kinematic Models

To answer this, we constructed simple kinematic models of disk and bulge populations as described in Morrison et al. (2003a). Briefly, for each PN, X and Y are known, but the line-of-sight depth is not. Using a Monte Carlo method, we choose a likely line-of-sight position based on the density distribution and iterate until a detectable PN results. Once we have a line-of-sight depth, we randomly generate an appropriate velocity for that position in the disk. The velocity is then projected into the line of sight. The result is a predicted velocity for each PN position given a specific kinematic model.

For the thin and thick disks, we assume an exponential surface brightness distribution in R and Z ;

$$L(R, z) = e^{(-R/h_r)} e^{(-z/h_z)}$$

where R is the cylindrical radius and z is the height above the galaxy plane.

For disk parameters of scale height, scale length and maximum radius, we have used the Milky Way and other spiral galaxies as templates. We adopted a scale height h_z of 0.3 kpc for the thin disk, comparable to that of the Milky Way thin disk. For the thick disk, we chose a scale height of 1 kpc; increasing this to 2 kpc has no effect on our conclusions. The thin and thick disk scale length h_r and maximum radius are fixed at 5.9 kpc and 26 kpc respectively, values taken from WK88 and scaled for our assumed distance to M31 of 770 kpc. Although thick disks in other galaxies have larger scale lengths than the thin disks (Morrison 1999; Neeser, Sackett, De Marchi, & Paresce 2002), varying the thick disk scale length by 20% had no measurable effect on the models we discuss in the next section. Thus far, the few attempts to constrain the cutoff radius of thick disks suggest that thin and thick disks in a given galaxy have the same extent (Pohlen, Balcells, Lütticke, & Dettmar 2004).

At the large values of X under consideration, v_{rot} can be treated as constant, and we fix v_{circ} at 250 km/s, a representative value based on the HI data. We have adopted a relationship between v_{circ} and σ_r derived from the van der Kruit & Freeman (1984) and Bottema (1993) studies of galaxy disks:

$$\sigma_r = \frac{1}{3}v_{circ}e^{-R/2h_r}$$

This relationship can be normalized to match the Milky Way thin and thick disk values of σ_r at the solar radius, taken from reviews by Norris (1999) and Morrison (1999) and listed in Table 4. The equation becomes:

$$\sigma_r = \sqrt{h_z}v_{circ}e^{-R/2h_r}$$

The velocity ellipsoid follows from the epicycle approximation (e.g. Binney & Tremaine 1987):

$$(\sigma_r, \sigma_\phi, \sigma_z) = \left(\sigma_r, \frac{\sigma_r}{\sqrt{2}}, \frac{\sigma_r}{2}\right)$$

For the bulge model, we use an $R^{1/4}$ surface brightness profile, with an axial ratio of $b/a=0.55$ (PvdB), and adopt an isotropic velocity ellipsoid ($\sigma_\phi = \sigma_z = \sigma_r$), with constant rotation at these large values of X . This simplification is not unreasonable. As yet, little is known about the behavior of bulges at large radii; some bulges exhibit cylindrical rotation, while others show a decrease in v_{rot} with distance from the midplane (Kormendy & Illingworth 1982). In the current sample, there are too few PN to test a more detailed model.

We have chosen an axisymmetric model for the bulge, although some authors suggests that M31’s inner bulge is triaxial (Braun 1991; Stark & Binney 1994; Berman & Loinard 2002). We note that the 2MASS image of the M31 bulge (Jarrett et al. 2003) shows considerably less isophote twisting than the optical images, suggesting that the disk warp may have contributed to earlier impressions of a triaxial bulge. The HI rotation curve of Braun (1991) shows a strong central peak which he attributes to non-circular gas orbits, suggesting a triaxial potential. However, the CO rotation curve of Loinard et al. (1999) has a smaller central peak than the HI curve of Braun (1991). Thus, the bulge may not be strongly triaxial.

3.4.2. Modeling Results

Representative thin disk, thick disk, and bulge models for the outer PN are shown with the data for comparison in Figure 9. The important properties of these models are summarized in Table 5. Only a small fraction of the PN have positions which can be fit by the thin disk model. Most of the PN (20 of 33) at $|Y| > 6$ would deproject to radii beyond the optical edge of the disk at 25–35 kpc. Perhaps more convincingly, the PN velocities are also incompatible with this model. Because velocity dispersion falls off with radius in a disk of constant scale height (van der Kruit & Freeman 1984; Bottema 1993) and is low ($\sim 20-30$

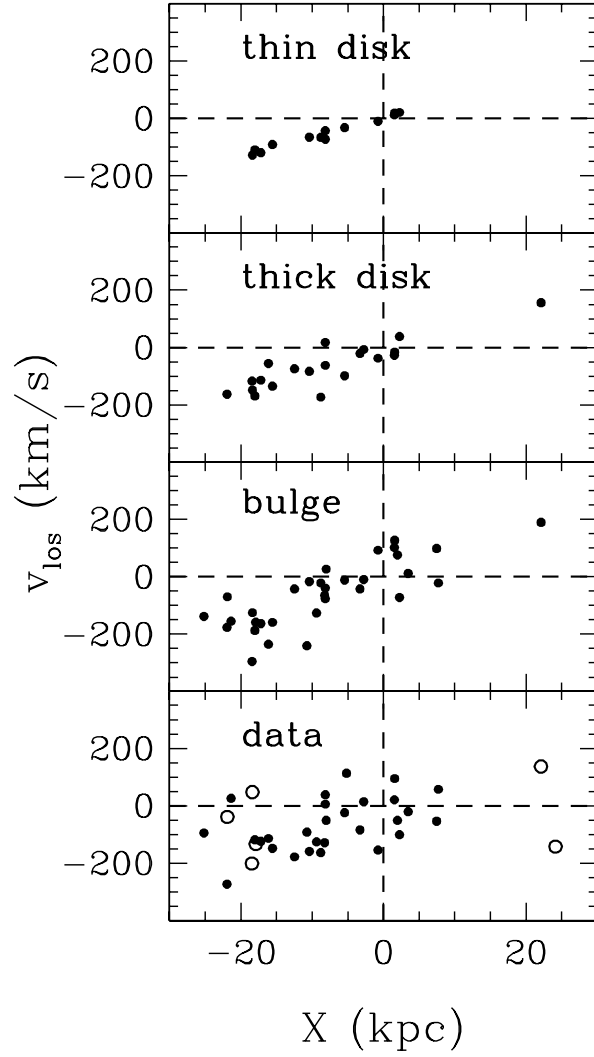


Fig. 9.— A comparison of thin disk, thick disk, and bulge kinematic models and the PN kinematics, for $|Y| > 6$. Solid circles are PN from this survey, and open circles are PN from NF87. Both the thin and thick disk kinematics have less dispersion at this height above the major axis than the data.

km/s) for a thin disk at all radii, the disk at this large radius has a low line-of-sight velocity dispersion. This kinematic discrepancy between the model and the data holds regardless of the maximum radius of the model disk used.

The thick disk model could account for the PN at $|Y| = 6 - 10$ kpc; however, the velocity dispersion along the minor axis in the model is significantly less than observed, because PN this far from the major axis would belong to the outer disk where the dispersion is relatively low. By 25 kpc, σ_r has fallen to < 40 km/s in our model of the thick disk. The contribution of the thick disk is vanishingly small by $|Y| = 10$ kpc, and the thirteen PN beyond this (see Figure 5) are not fit by the thick disk model. Those thirteen PN have a significant rotation component, with an average v_{los} of ~ 70 km/s.

Occam’s razor is an appropriate consideration here – there is no need to introduce a new stellar population in M31. The thirteen PN beyond $|Y| = 10$ kpc already represent a rotating population which are not explained by the thick disk model. No convincing evidence of a thick disk in M31 has yet emerged, and the cold kinematics of many M31 clusters suggests that M31 has not experienced a merger massive enough to form a thick disk since the birth of the globular clusters (Morrison et al. 2003b); only satellites with $\sim 10\%$ of the disk mass significantly heat the disk (Quinn & Goodman 1986; Walker, Mihos, & Hernquist 1996).

The bulge, however, offers a ready explanation. Existing star counts have already hinted that the bulge extends far into the canonical halo. The minor axis profile is well-fit by a single $R^{1/4}$ profile as far out as it has been measured (20 kpc; PvdB). In Figure 10, we have binned the complete subsample of Field 1 PN along the minor axis ($|X| < 3$ kpc) by isophotal radius, assuming that the bulge has an axial ratio of 0.55. We determined the complete subsample by fitting the known PN luminosity function to the histogrammed data, similar to Ciardullo et al. (1989). At some point, the number of PN observed falls off from the predicted number of PN and this determines our completeness limit. The two PN from Field 2 which are included in this minor axis sample are the two most distant bins in the histogram. The inner three bins are affected by our exclusion of PN very near the center of the galaxy, as described earlier.

The minor axis PN distribution is well fit by the prediction of the PvdB surface brightness profile, assuming the M31 PN production rate of Ciardullo et al. (1989) for the upper ~ 1.5 magnitudes of the PN luminosity function. It has been suggested that a drop in the PN production rate can be caused by both extreme old age and very low metallicity (Ciardullo 1995; Jacoby et al. 1997; Magrini et al. 2003), as expected in a halo population. We see no dramatic change, however, in the PN production rate along the minor axis out to at least 12 kpc. This suggests no sudden decrease in metallicity or age of the dominant population, but rather continuity from the central bulge out to at least 12 kpc.

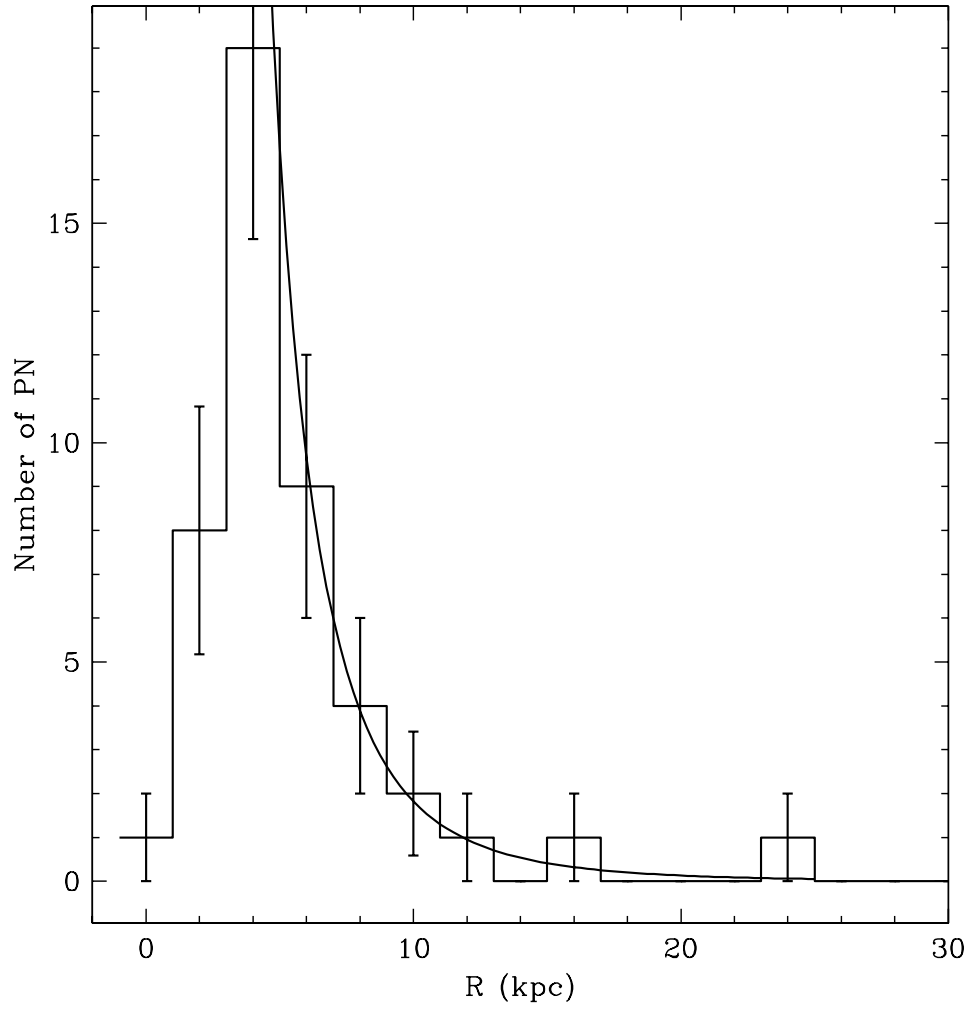


Fig. 10.— The distribution of PN along the minor axis. PN in the complete subsample within 3 kpc of the minor axis are assigned an isophotal distance and binned into 2 kpc bins. The solid line is the number of PN expected based on the minor axis surface brightness profile from PvdB, normalized to the depth of our survey. The first three bins are reduced by our exclusion of PN near the center of the galaxy.

With this in mind, we feel justified in considering whether the outer PN velocities are consistent with bulge kinematics. Like the bulges of other early-type spirals, which have $v/\sigma_v \sim 1$ (Kormendy & Illingworth 1982; Davies & Illingworth 1983), M31 has a moderate degree of rotational support in the inner regions. The central bulge has a large velocity dispersion (100 km/s) and a rotation curve which rises to 80 km/s by about 1 kpc (Richstone & Shtetman 1980). This is significantly less rotation than seen in the data (116 km/s), and a kinematic model based on the central bulge characteristics proves incompatible with our data (Figure 11).

However, this is not a fair comparison. The properties of the central bulge are based on the nuclear observations of Richstone & Shtetman (1980) and the stellar absorption data of McElroy (1983), which only extend to about 2 kpc along the major axis, less than 1 R_e for the M31 bulge. These data are on the rising portion of McElroy’s rotation curve, and in fact show an increase in mean velocity with distance from the center in his Figure 7. Therefore, the bulge rotation could reasonably flatten out at 150 to 200 km/s beyond 6 kpc on this side of the galaxy.

Recent observations of low luminosity ellipticals (Rix, Carollo, & Freeman 1999) show a similar increase in the degree of rotational support at large radii ($> 1R_e$), with $v/\sigma = 2-3$ in many cases. M31’s bulge occupies the same region of the fundamental plane as low luminosity ellipticals (Kormendy 1985, 1987; Kormendy & Bender 1999), and we might therefore expect that they have common kinematic properties.

The low-luminosity elliptical data are derived from stellar absorption spectra along the major axis, while our outer PN are far off-axis. In order to make a better comparison, we have used our kinematic models to predict the value of v_{rot} and σ_r that we would expect to observe along the major axis if our PN belong to a bulge with increasing rotational support. We generated 1000 realizations for each of a set of models covering a range of possible v_{rot} and σ_r values, and compared the resulting probability distributions for our variables to our observed values.

We found from our models that the line-of-sight dispersion is independent of the rotation velocity in the range of interest, and that $\sigma_r = 50 - 90$ km/s bracketed the range of reasonable values (Figure 12). For those values, $v_{rot} = 130$ to 170 km/s matched v_{los} (Figure 13). Our final best estimate is $v_{rot} = 150 \pm 20$ km/s and $\sigma_r = 70 \pm 20$ km/s, where the uncertainties cover the range of model parameters that led to a match with the measured values of v_{los} and σ_{los} . In the lower right panel of Figure 6, we have plotted the range of velocities generated for each PN position in the 1000 model runs of this best model. Only one outer PN is never fit by the bulge model, in contrast to the disk models. The dark line is the average rotation curve for all the PN with $|Y| > 6$, and the lighter lines are the model 10% confidence limits for

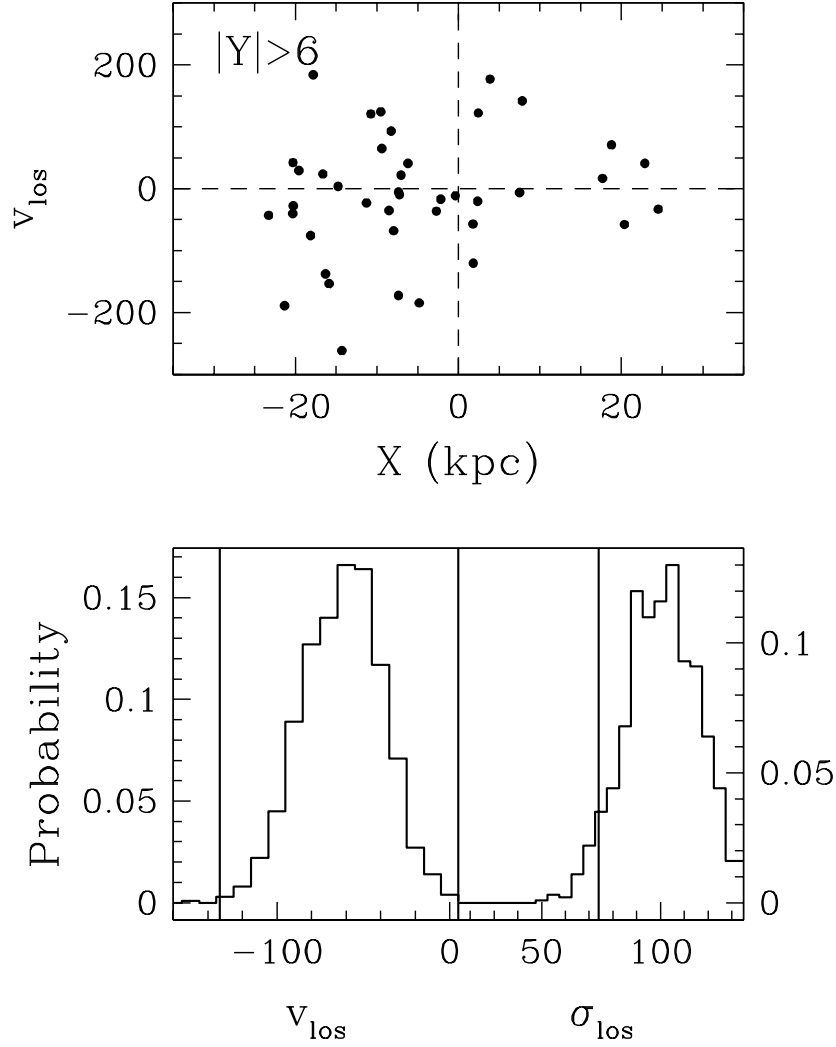


Fig. 11.— Upper panel: One realization of a bulge model with $v_{rot} = 80$ km/s and $\sigma_r = 100$ km/s. Lower panel: The probability distribution for the mean v_{los} and for σ_{los} measured from the positions at $|Y| > 6$ and $|X| > 10$ for 1000 realizations of the same bulge model as in the upper panel. The solid lines represent the values measured from the data, $v_{los} = 116$ km/s and $\sigma_{los} = 79$ km/s. All velocities are in km/s.

these PN. Most fall within the limits – their velocities are consistent with our bulge model.

Interestingly, Reitzel et al. (2004) find evidence of a population with similar rotation in a field 34 kpc along the major axis. Roughly two-thirds of their sample of 23 M31 red giants have velocities relative to M31 of 150 km/s, in good agreement with our model-based estimate for the major axis rotation for the outer bulge. However, the dispersion is low, only 27 km/s, and Reitzel et al. (2004) reason that these giants may belong to the disk, or cold substructure in the halo. More velocities covering a wider area will be needed to disentangle these populations.

For the outer PN, the model suggests $v/\sigma = 150/70 = 2.1^4$, well within the range covered by the low-luminosity ellipticals (Rix, Carollo, & Freeman 1999). If we accept that these PN belong to the M31 bulge based on the surface brightness profile, then the velocities imply that M31’s bulge shares kinematic as well as photometric properties with low luminosity ellipticals. This strengthens the evolutionary connection between these types of galaxies, and may provide an important clue to understanding the formation of large spirals like M31.

3.5. The Halo

Regardless of how we interpret the large rotation velocity of the outer PN, it seems clear that most do not belong to a kinematically hot, canonical halo. Are there any PN in our sample which could? Without recourse to more detailed models than justified by the data, the best we can do is identify PN which cannot belong to either the disk or the bulge. At all Y , a few objects can be found that have velocities which are inconsistent with either of these populations, and their coordinates and velocities are listed in Table 6. As a group, their spectra do not systematically differ from the other PN.

The suprising conclusion we draw from the PN velocities and Figure 14, where we have overplotted their positions on Figure 2 from Ferguson et al. (2002), is that all five halo PN probably belong to tidal streams in M31’s outer halo. One is projected on the Northern spur, and is counter-rotating with respect to the disk there. Two are projected near the major axis at $X = -10$ kpc; their velocities are similar to M32’s systemic velocity and they could be debris from that galaxy. All three of these halo PN have velocities in the “forbidden” quadrants.

The remaining two halo PN are located near the center of the galaxy. Their velocities

⁴We use v/σ in the same sense as Rix, Carollo, & Freeman (1999): a simple quotient of the line-of-sight velocity and velocity dispersion at a given position

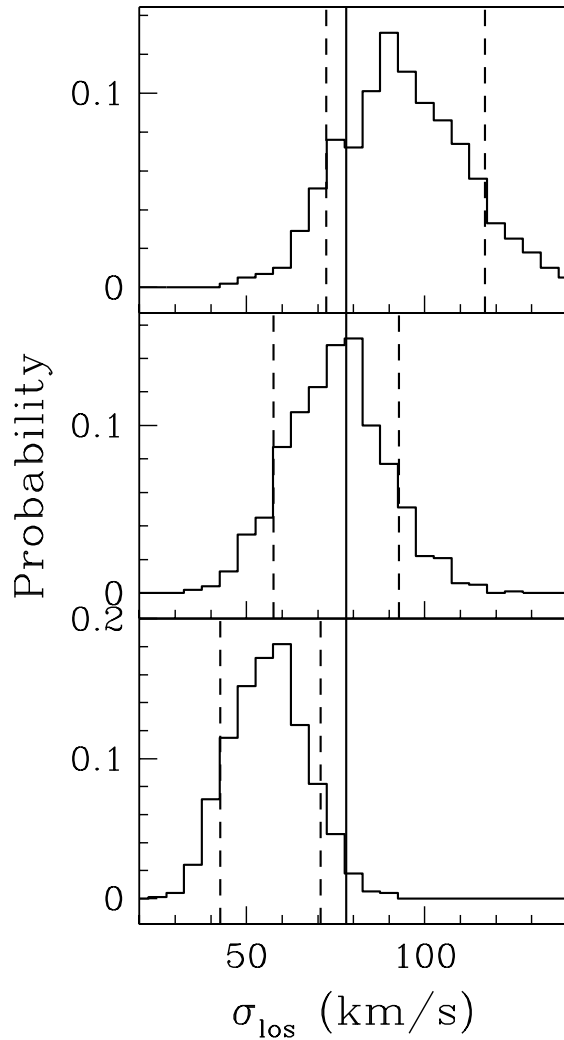


Fig. 12.— The probability distribution for σ_{los} measured from the positions at $|Y| > 6$ and $|X| > 10$ for 1000 realizations of various bulge models. The solid lines represent the value from the data, $\sigma_{los} = 79$ km/s, and the dashed lines are the 10% confidence limits from the models. Upper panel: a model bulge with $v_{rot} = 160$ km/s and $\sigma_r = 90$ km/s. Middle panel: a model bulge with $v_{rot} = 160$ km/s and $\sigma_r = 70$ km/s. Lower panel: a model bulge with $v_{rot} = 160$ km/s and $\sigma_r = 50$ km/s.

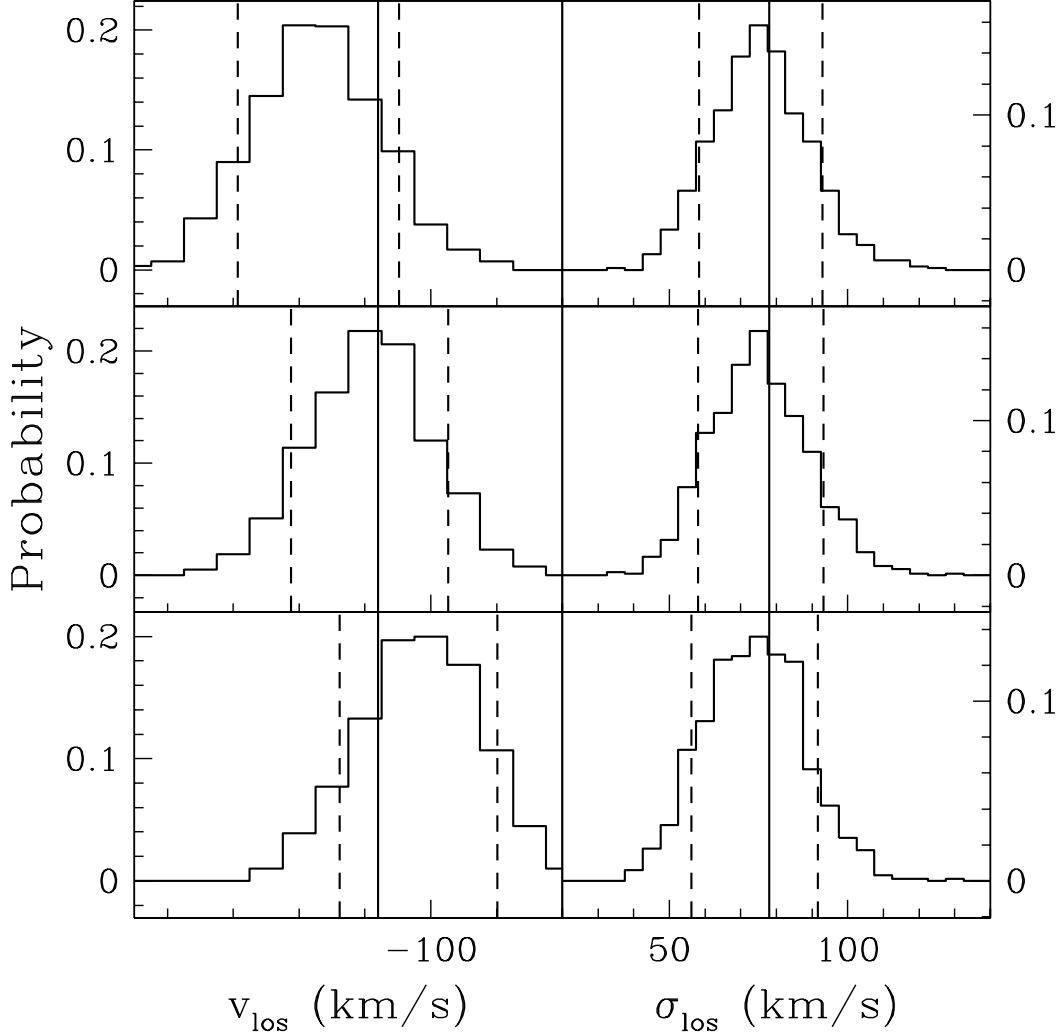


Fig. 13.— The probability distribution for the mean v_{los} and for σ_{los} measured from the positions at $|Y| > 6$ and $|X| > 10$ for 1000 realizations of various bulge models. The solid lines represent the values from the data, $v_{los} = 116$ km/s and $\sigma_{los} = 79$ km/s, and the dashed lines are the 10% confidence limits from the models. Upper panel: a model bulge with $v_{rot} = 170$ km/s and $\sigma_{los} = 70$ km/s. Middle panel: a model bulge with $v_{rot} = 150$ km/s and $\sigma_r = 70$ km/s. Lower panel: a model bulge with $v_{rot} = 130$ km/s and $\sigma_r = 70$ km/s.

are within 40 km/s of each other ($v_{helio} \sim -600$ km/s) and are at least 3 times the central bulge dispersion (100 km/s). Orbits suggested by Merrett et al. (2003) and Ibata et al. (2004) for the Southern Stream (Ibata et al. 2001; Ferguson et al. 2002) project near the position of these PN. Their velocities follow the gradient found by Ibata et al. (2004), implying that these PN could belong to the Southern Stream. Finding PN in low surface brightness streams is somewhat unexpected, as PN are intrinsically rare objects (only $\sim 30/10^9 L_{\odot}$; Ciardullo et al. 1989). Velocities in the streams will provide constraints on the orbits of their progenitors, and deeper observations are planned to detect more stream PN. We will revisit these possible streams in a later paper.

We have yet to find the M31 analog to the hot component of the Milky Way inner halo. If the PN production rate per unit luminosity is the same as for other M31 populations, we would expect to see of order 20–30 PN if we covered the entire halo of M31 at the depth of our survey and its luminosity is of order $10^9 L_{\odot}$, the approximate luminosity of the Milky Way halo (Morrison & Harding 1993). Depending on the density distribution of the halo stars, we have surveyed one quarter or less of the halo, so very roughly 5–7 PN would be expected in our sample from such a halo. Yet all 5 of our halo PN candidates belong to kinematically cold features in the halo.

On the surface, this suggests that the M31 halo does not have a kinematically hot component analogous to the inner Milky Way halo. However, if the hot component of the M31 halo is as old and metal-poor as the Milky Way halo, the PN production rate could be lower by a factor of 5 or more (Magrini et al. 2003). This would be consistent with a total lack of hot halo objects in our sample. Studies in search of these objects must reach farther down the PN luminosity function by several magnitudes.

Spectroscopic surveys of red giant stars, because of the larger sample size, may be needed to find the hot halo, especially if the PN production rate is significantly lower for old populations. Reitzel & Guhathakurta (2002) found a high dispersion of 150 km/s in a sample of M31 red giants in a field 19 kpc along the minor axis. This field is further out than our PN sample and may have reached, at last, a region where the halo dominates.

4. Discussion

4.1. Bulge vs. Halo

The extent of M31’s bulge has been a topic of debate in the literature. Some previous studies of M31 stellar populations suggested that fields as far out as 20 kpc were still dominated by the bulge (Mould & Kristian 1986; Durrell et al. 2001; Freeman 1996) primarily

because of two important findings: first, the higher metallicity of the stars compared to the Milky Way halo at comparable radius (Durrell et al. 1994, 2001; Holland, Fahlman, & Richer 1996), and second, its $R^{1/4}$ surface brightness profile which extends smoothly out to at least 20 kpc on the minor axis (PvdB). We add to this evidence the discovery that PN at $|Y| > 6$ kpc, in regions typically associated with the halo, have a $v_{los} = 116$ km/s and $\sigma_{los} = 79$ km/s. This rotation is very different from the behavior of the Milky Way halo populations at similar radii and suggests that the bulge light dominates even out to 20 kpc on the minor axis.

M31 globular clusters also differ significantly from their Milky Way counterparts. As a system, the clusters have a large rotation, ~ 150 km/s on average (Perrett et al. 2002). This holds for both the metal-rich and the metal-poor subsets, implying that neither have clear “halo” kinematics, although the precise velocity dataset of Perrett et al. (2002) was confined to inner regions and may select against halo objects. Morrison et al. (2003a) demonstrate that $\sim 50\%$ of M31 clusters projected on the disk actually have thin disk kinematics. No analogous population is known among the Milky Way globular clusters. In contrast, studies of the Milky Way globular clusters have found that metal-poor clusters belong to the halo (Zinn 1985), while the central *metal-rich* clusters have either bulge or thick disk kinematics (Frenk & White 1982; Minniti 1995; Côté 1999; Armandroff 1989).

If canonical M31 halo regions are actually dominated by the bulge, then further comparisons with the Milky Way *halo* are misleading. Instead, these M31 halo regions provide a baseline for comparison to more distant early type spiral bulges. How does a bulge with moderate rotational support form? In major mergers, angular momentum can migrate outwards in the dark halo as it is assembled (Quinn & Zurek 1988). Thus, a bulge which formed in the very early stages of galaxy formation simultaneously with the dark halo assembly would have the $R^{1/4}$ law profile characteristic of violent relaxation as well as increased rotation at large radii. PN studies of the outer regions of some large ellipticals show this expected increase in rotation with radius (e.g. Hui et al. 1993).

Dissipationless mergers of disk galaxies of unequal mass (ratio 3:1) can also lead to disky remnants with more rotational support in the inner regions and $R^{1/4}$ law profiles (Naab, Burkert, & Hernquist 1999; Bendo & Barnes 2000) as the larger disk partly survives the interaction. We find that the kinematics of M31’s outer bulge is in rough agreement with the low-luminosity elliptical observations. A comparison of M31’s bulge kinematics with these observations is complicated because velocities for the ellipticals were measured along the major axis. Nonetheless, we find that $v/\sigma = 2.1$ by $5R_e$, based on the outer bulge PN kinematics in M31 (assuming $R_e = 2.4$ kpc on the major axis; PvdB), similar to values for the low luminosity ellipticals, suggesting an evolutionary kinship.

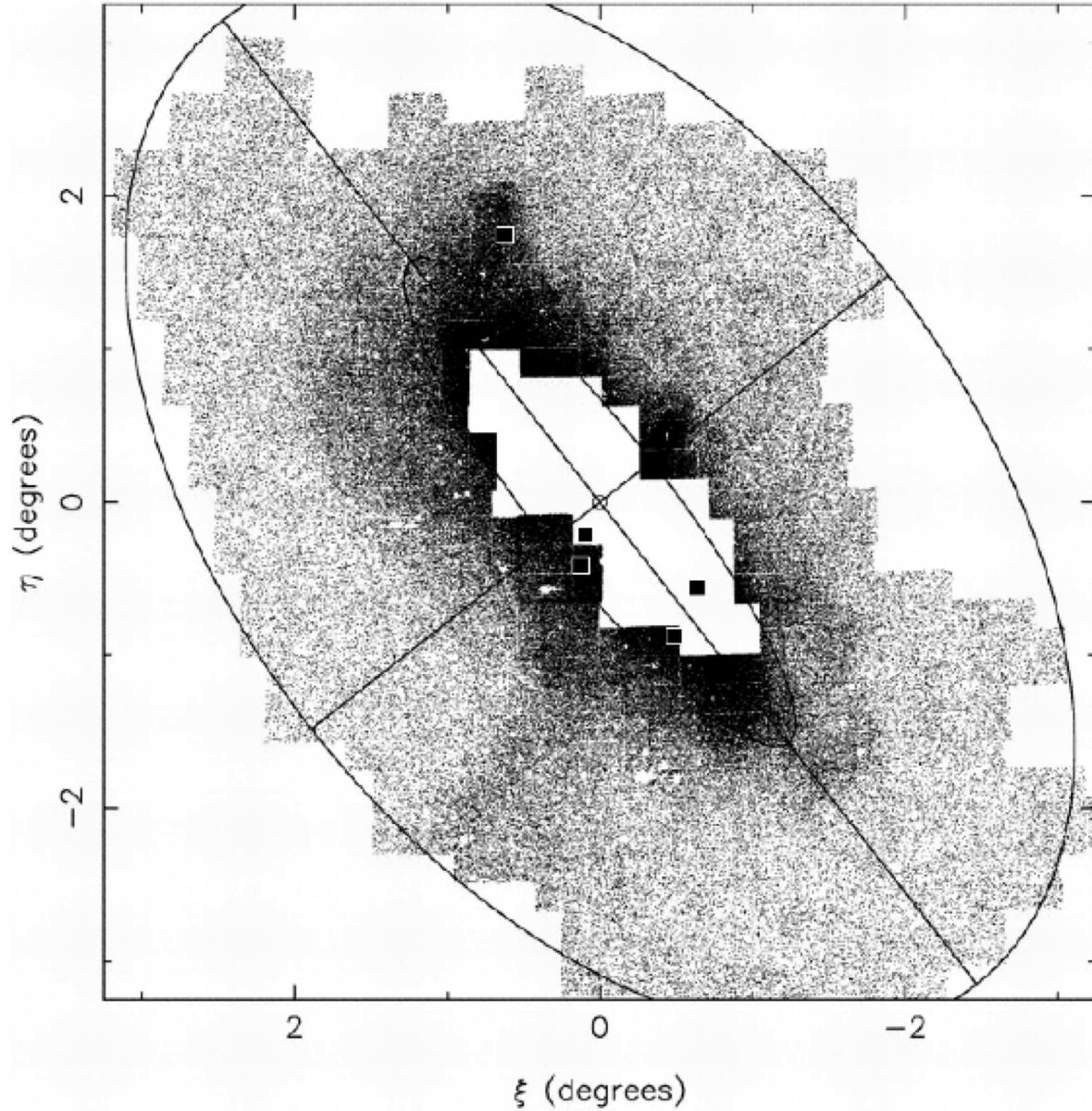


Fig. 14.— Figure 2 from Ferguson et al. 2002, showing M31’s halo and tidal streams, with the positions of our potential halo objects marked (red in the electronic edition). All 5 fall on or near possible tidal streams, and three are counter-rotating with respect to the disk at their position. The two halo candidates near the center have velocities within 40 km/s of each other, and have velocities relative to M31 which are at least 3 times the central bulge dispersion. Orbits suggested by Merrett et al. (2003) and Ibata et al. (2004) for the Southern Stream (Ibata et al. 2001; Ferguson et al. 2002) project near the position of these PN.

4.2. The Elusive Halo Remains Elusive

In our entire survey, we only find a handful of PN in the combined sample with halo-like kinematics. Ideally, these are the sample we should compare to the Milky Way halo; however, our PN spectra are not suitable for abundances, and tell us nothing about ages. In principle, they offer the possibility of comparing the luminosities of the M31 and Milky Way halos, because the PN are direct tracers of the underlying stars. However, this is a difficult comparison to make for several reasons. First, uncertainties in the PN production rate make it difficult to translate the number of PN to stellar luminosity. Second, hot halo objects can have any velocity, and confusion with the disk and bulge prevent us from unambiguously identifying those not in the forbidden quadrants. Third, the Milky Way halo luminosity is only approximately known, and depends strongly on the density of the little-studied inner halo, because the halo density distribution is extremely centrally concentrated, with a globular cluster density proportional to $r^{-3.5}$ (Zinn 1985).

Perhaps most important, a generalization from our survey to the entire halo is not appropriate if M31’s halo is clumpy. In fact, we know this to be an important issue, as substructure in field star counts has been detected in M31’s halo (Ibata et al. 2001; Ferguson et al. 2002). The clumpiness of the Milky Way halo is now accepted, based on the disruption of the Sgr dSph (Ibata et al. 1994; Ivezić et al. 2000; Yanny et al. 2000; Dohm-Palmer et al. 2001) and on studies of velocity substructures among the metal-poor halo giants in the solar neighborhood (Helmi et al. 1999).

The PN observations thus far tell us more about the bulge than the halo, as do other studies of the stellar populations in these fields. The results of such studies can now be associated with the bulge; for example, estimates of a surprisingly high halo luminosity (Reitzel, Guhathakurta, & Gould 1998), an intermediate-age component (Brown et al. 2003), and moderate flattening (PvdB; Ferguson et al. 2000).

5. Summary

Our search for M31’s halo has led to a picture of that galaxy very different from that of the Milky Way. PN at large distances from the M31 major axis have significant rotation and small velocity dispersion, in contrast to the large velocity dispersion of the Milky Way halo. We conclude that these objects do not belong to the halo, but to the outer reaches of the bulge.

If this is the case, then among other characteristics, M31’s bulge shares the rotation properties of low-luminosity ellipticals; namely, that the amount of rotational support in-

creases with radius. This suggests an evolutionary kinship with low-luminosity ellipticals, which are believed to have formed via hierarchical merging of objects of nearly equal mass, in contrast to the Milky Way halo which formed from the on-going accretion of very small satellites.

Any kinematically hot halo in M31 is represented by a very small number of objects in our sample. Yet given the rarity of PN, even these few could imply a halo luminosity comparable to that of the Milky Way, if they belong to a smooth inner component. However, their projection on M31 suggest they may instead belong to tidal streams in a clumpy halo. We are not claiming that that M31 does not have a Milky-Way like halo. Rather we support, as some earlier researchers have surmised, that the halo is dominated by the bulge out to 20 kpc and farther; preliminary star counts of red giants in a field at 30 kpc reveal a similar metallicity distribution function to that of nearer regions (P. Durrell 2003, private communication).

Sorting out M31’s evolutionary history will require more data, and PN provide the means. With a larger sample of PN velocities, we can clarify the distinction between bulge and halo by connecting the kinematics to the spatial distribution. Most important, abundances can be derived for our sample of halo objects. This is a great advantage of PN; they can ultimately provide a large number of abundances (e.g. Jacoby & Ciardullo 1999), where this is costly in telescope time for field stars (Reitzel & Guhathakurta 2002). The ability to tie abundance to kinematics is a connection which has been critical to our understanding of the stellar populations of the Milky Way.

6. Acknowledgements

We thank Rene Walterbos for providing the surface photometry of M31 and the image used in Figure 2; Annette Ferguson for the use of Figure 2 from Ferguson et al. (2002); John Feldmeier and Chris Mihos for many useful discussions. H.L.M acknowledges the support of NSF CAREER grant AST-9624542. D.H.K. is supported by an NSF Astronomy and Astrophysics Postdoctoral Fellowship under award AST-0104455.

REFERENCES

- Armandroff, T. E. 1989, *AJ*, 97, 375
Arnaboldi, M. et al. 1996, *ApJ*, 472, 145

- Arnaboldi, M., Freeman, K. C., Gerhard, O., Matthias, M., Kudritzki, R. P., Mendez, R. H., Capaccioli, M., & Ford, H. 1998, *ApJ*, 507, 759
- Barmby, P., Huchra, J. P., Brodie, J. P., Forbes, D. A., Schroder, L. L., & Grillmair, C. J. 2000, *AJ*, 119, 727.
- Beers, T. C., Chiba, M., Yoshii, Y., Platais, I., Hanson, R. B., Fuchs, B., & Rossi, S. 2000, *AJ*, 119, 2866
- Bendo, G. J. & Barnes, J. E. 2000, *MNRAS*, 316, 315
- Berman, S. & Loinard, L. 2002, *MNRAS*, 336, 477
- Binney, J. & Tremaine, S. 1987, *Galactic Dynamics* (Princeton: Princeton University Press)
- Bottema, R. 1993, *A&A*, 275, 16
- Braun, R. 1991, *ApJ*, 372, 54
- Brinks, E. & Shane, W. W. 1984, *A&AS*, 55, 179
- Brinks, E. & Burton, W. B. 1984, *A&A*, 141, 195
- Brown, T. M., Ferguson, H. C., Smith, E., Kimble, R. A., Sweigart, A. V., Renzini, A., Rich, R. M., & VandenBerg, D. A. 2003, *ApJ*, 592, L17
- Ciardullo, R., Jacoby, G. H., Ford, H. C., & Neill, J. D. 1989, *ApJ*, 339, 53
- Ciardullo, R. 1995, in *IAU Highlights of Astronomy 10*, ed. I. Appenzeller (Dordrecht:Kluwer), 507
- Côté, P. 1999, *AJ*, 118, 406
- Courteau, S., de Jong, R. S., & Broeils, A. H. 1996, *ApJ*, 457, L73
- Couture, J., Racine, R., Harris, W. E., & Holland, S. 1995, *AJ*, 109, 2050
- Cram, T. R., Roberts, M. S., & Whitehurst, R. N. 1980, *A&AS*, 40, 215
- Cretton, N., Naab, T., Rix, H., & Burkert, A. 2001, *ApJ*, 554, 291
- Davies, R. L. & Illingworth, G. 1983, *ApJ*, 266, 516
- Deharveng, J. M. & Pellet, A. 1975, *A&AS*, 19, 351
- de Vaucouleurs, G. 1958, *ApJ*, 128, 465

- de Vaucouleurs G., de Vaucouleurs A., Corwin H. G., Jr., Buta, R. J., Paturel, G., & Fouqu, P. 1991, *Third Reference Catalogue of Bright Galaxies* (New York: Springer)
- Dohm-Palmer, R. C. et al. 2001, *ApJ*, 555, L37
- Dressler, A & Richstone, D. 1988, *ApJ*, 324, 701
- Drimmel, R., & Spergel, D. N., 2003, *ApJ*, 556, 181
- Durand, S., Acker, A., & Zijlstra, A. 1998, *A&AS*, 132, 13
- Durrell, P. R., Harris, W. E., & Pritchett, C. J. 1994, *AJ*, 108, 2114
- Durrell, P. R., Harris, W. E., & Pritchett, C. J. 2001, *AJ*, 121, 2557
- Durrell, P. R., Harris, W. E., & Pritchett, C. J. 2004, *AJ*, 128, 260
- Edvardsson, B., Andersen, J., Gustafsson, B., Lambert, D. L., Nissen, P. E., & Tomkin, J. 1993, *A&A*, 275, 101
- Eggen, O. J., Lynden-Bell, D., & Sandage, A. R. 1962, *ApJ*, 136, 748
- Ferguson, A. M. N., Gallagher, J. S., & Wyse, R. F. G. 2000, *AJ*, 120, 821
- Ferguson, A. M. N., Irwin, M. J., Ibata, R. A., Lewis, G. F., & Tanvir, N. R. 2002, *AJ*, 124, 1452
- Ford, H. C., Jacoby, G., & Jenner, D. C. 1977, *ApJ*, 213, 18
- Freedman, W. L. & Madore, B. F. 1990, *ApJ*, 365, 186
- Freeman, K. C. 1987, *ARA&A*, 25, 603
- Freeman, K. C. 1988, *IAU Symp. 130: Large Scale Structures of the Universe*, 130, 301
- Freeman, K. C. 1996, *ASP Conf. Ser. 92: Formation of the Galactic Halo...Inside and Out*, 3
- Frenk, C. S. & White, S. D. M. 1982, *MNRAS*, 198, 173
- Gilmore, G. & Reid, N. 1983, *MNRAS*, 202, 1025
- Helmi, A., White, S. D. M., de Zeeuw, P. T., & Zhao, H. 1999, *Nature*, 402, 53
- Holland, S., Fahlman, G. G., & Richer, H. B. 1996, *AJ*, 112, 1035

- Huchra, J. P., Brodie, J. P., & Kent, S. M. 1991, *ApJ*, 370, 495
- Huchra, J. P. 1993, *ASP Conf. Ser.* 48: The Globular Cluster-Galaxy Connection, 420
- Huchra, J. P., Vogeley, M. S. & Geller, M. J. 1999, *ApJS*, 121, 287
- Hui, X., Ford, H. C., Ciardullo, R. & Jacoby, G. H. 1993, *ApJ*, 414, 463
- Hui, X., Ford, H., Jacoby, G. 1994, *AAS*, 26, 938
- Hui, X., Ford, H. C., Freeman, K. C., & Dopita, M. A. 1995, *ApJ*, 449, 592
- Ibata, R. A., Gilmore, G., & Irwin, M. J. 1994, *Nature*, 370, 194
- Ibata, R., Irwin, M., Lewis, G., Ferguson, A. M. N., & Tanvir, N. 2001, *Nature*, 412, 49
- Ibata, R., Chapman, S., Ferguson, A. M. N., Irwin, M., Lewis, G., & McConnachie, A. 2004, preprint (astro-ph/0403068)
- Ivezić, Z. et al. 2000, *AJ*, 120, 963
- Jacoby, G. H., Ciardullo, R., Booth, J., & Ford, H. C. 1989, *ApJ*, 344, 704
- Jacoby, G. H. et al. 1992, *PASP*, 104, 599
- Jacoby, G. H., Morse, J. A., Fullton, L. K., Kwitter, K. B., & Henry, R. B. C. 1997, *AJ*, 114, 2611
- Jacoby, G. H. & Ciardullo, R. 1999, *ApJ*, 515, 169
- Jarrett, T. H., Chester, T., Cutri, R., Schneider, S. E., & Huchra, J. P. 2003, *AJ*, 125, 525
- Kent, S. M. 1989, *AJ*, 97, 1614
- Kormendy, J. & Illingworth, G. 1982, *ApJ*, 256, 460
- Kormendy, J. 1985, *ApJ*, 295, 73
- Kormendy, J. 1987, *Nearly Normal Galaxies. From the Planck Time to the Present*, 163
- Kormendy, J. 1988, *ApJ*, 325, 128
- Kormendy, J. & Bender, R. 1999, *ApJ*, 522, 772
- Kulkarni, S. R., Heiles, C. & Blitz, L. 1982, *ApJ*, 259L, 63
- Laird, J. B., Carney, B. W., Rupen, M. P., & Latham, D. W. 1988, *AJ*, 96, 1908

- Loinard, L., Dame, T. M., Heyer, M. H., Lequeux, J., & Thaddeus, P. 1999, *A&A*, 351, 1087
- Lopez-Corredoira, M., Cabrera-Lavers, A., Garzon, F., & Hammersly, P. L., 2002, *A&A*, 394, 883
- Magrini, L. et al. 2003, astro-ph/0305105
- Majewski, S. R., Munn, J. A., & Hawley, S. L. 1994, *ApJ*, 427, L37
- Mateo, M. L. 1998, *ARA&A*, 36, 435
- McElroy, D. B. 1983, *ApJ*, 270, 485
- Méndez, R. H., Riffeser, A., Kudritzki, R.-P., Matthias, M., Freeman, K. C., Arnaboldi, M., Capaccioli, M., & Gerhard, O. E. 2001, *ApJ*, 563, 135
- Merrett, H. R., et al. 2003, *MNRAS*, 346, 62
- Minniti, D. 1995, *AJ*, 109, 1663
- Monet, D. et al. 1998, *The USNO-A2.0 Catalogue*, (U.S. Naval Observatory, Washington DC)
- Morrison, H. L. & Harding, P. 1993, *PASP*, 105, 977
- Morrison, H. L., Boroson, T. A., & Harding, P. 1994, *AJ*, 108, 1191
- Morrison, H. L., Miller, E. D., Harding, P., Stinebring, D. R., & Boroson, T. A. 1997, *AJ*, 113, 2061
- Morrison, H. L. 1999, *ASP Conf. Ser. 165: The Third Stromlo Symposium: The Galactic Halo*, 174
- Morrison, H. L., Harding, P., Jacoby, G. & Hurley-Keller, D. A., *ApJ*, in press
- Morrison, H. L., Harding, P., Jacoby, G. & Hurley-Keller, D. A., *ApJ*, in press
- Mould, J. 1986, *Stellar Populations*, 9
- Mould, J. & Kristian, J. 1986, *ApJ*, 305, 591
- Naab, T., Burkert, A., & Hernquist, L. 1999, *ApJ*, 523, L133
- Neeser, M. J., Sackett, P. D., De Marchi, G., & Paresce, F. 2002, *A&A*, 383, 472
- Nolthenius, R. & Ford, H. 1986, *ApJ*, 305, 600

- Nolthenius, R. & Ford, H. C. 1987, *ApJ*, 317, 62. (NF87)
- Norris, J. 1986, *ApJS*, 61, 667
- Norris, J. 1999, *Ap&SS*, 265, 213
- Oey, M. S. 2000, *ApJ*, 542L, 25
- Olling, R. 1996, *AJ*, 112, 457
- Pellet, A., Astier, N., Viale, A., Courtes, G., Maucherat, A., Monnet, G., & Simien, F. 1978, *A&AS*, 31, 439
- Perrett, K. M., Bridges, T. J., Hanes, D. A., Irwin, M. J., Brodie, J. P., Carter, D., Huchra, J. P., & Watson, F. G. 2002, *AJ*, 123, 2490
- Pfenniger, D. & Norman, C. 1990, *ApJ*, 363, 391
- Pohlen, M., Balcells, M., Lütticke, R., & Dettmar, R. J. 2004, *A&A*, 422, 465
- Pritchett, C. J. & van den Bergh, S. 1994, *AJ*, 107, 1730
- Quinn, P. J. & Goodman, J. 1986, *ApJ*, 309, 472
- Quinn, P. J. & Zurek, W. H. 1988, *ApJ*, 331, 1
- Reitzel, D. B., Guhathakurta, P., & Gould, A. 1998, *AJ*, 116, 707
- Reitzel, D. B. & Guhathakurta, P. 2002, *AJ*, 124, 234
- Reitzel, D. B., Guhathakurta, P., & Rich, R. M. 2004, *AJ*, in press
- Rich, R. M., Mighell, K. J., Freedman, W. L., & Neill, J. D. 1996, *AJ*, 111, 768
- Richstone, D. O. & Sackett, S. A. 1980, *ApJ*, 235, 30
- Rix, H., Carollo, C. M., & Freeman, K. 1999, *ApJ*, 513, L25
- Roberts, M. S. & Whitehurst, R. N. 1975, *ApJ*, 201, 327
- Ryan, S. G. & Norris, J. E. 1991, *AJ*, 101, 1865
- Saha, A. 1985, *ApJ*, 289, 310
- Sancisi, R. & Allen, R. J. 1979, *A&A*, 74, 73
- Schechter, P. L., Mateo, M., & Saha, A. 1993, *PASP*, 105, 1342

- Searle, L. & Zinn, R. 1978, ApJ, 225, 357
- Stark, A. A. & Binney, J. 1994, ApJ, 426L, 31
- van der Kruit, P. C. & Freeman, K. C. 1984, ApJ, 278, 81
- van der Kruit, P. C. & Searle, L. 1981, A&A, 95, 105
- Walker, I. R., Mihos, J. C., & Hernquist, L. 1996, ApJ, 460, 121
- Walterbos, R. A. M. & Kennicutt, R. C. 1988, A&A, 198, 61 (WK88)
- Weiland, J. L. et al. 1994, ApJ, 425, L81
- Yanny, B. et al. 2000, ApJ, 540, 825
- Zepf, S. E., Liu, M. C., Marleau, F. R., Sackett, P. D., & Graham, J. R. 2000, AJ, 119, 1701
- Zinn, R. 1985, ApJ, 293, 424
- Zucker, D., et al. 2004, preprint (astro-ph/0401098)

Table 1. Coordinates and heliocentric velocities for PN candidates in M31.

ID	RA (2000)	Dec (2000)	v_{helio}	v_{err}
HKPN 1	0:38:41.29	39:47:40.1	-532.3	4.0
HKPN 2	0:38:44.19	40:17:58.9	-452.8	5.1
HKPN 3	0:38:54.97	40:10:16.2	-362.1	1.9
HKPN 4	0:38:56.63	39:47:14.2	-425.1	12.6
HKPN 5	0:39:02.52	40:22:50.5	-511.2	3.1
HKPN 6	0:39:03.40	39:45:58.4	-484.0	3.4
HKPN 7	0:39:03.76	39:53:29.0	-477.9	3.5
HKPN 8	0:39:04.46	40:34:30.3	-512.3	3.0
HKPN 9	0:39:05.33	40:41:46.0	-378.6	5.3
HKPN 10	0:39:06.60	40:14:59.8	-548.2	4.3
HKPN 11	0:39:09.32	40:11:21.0	-428.2	2.5
HKPN 12	0:39:14.80	40:24:28.6	-325.5	6.4
HKPN 13	0:39:15.00	40:26:34.5	-522.1	5.9
HKPN 14	0:39:15.80	40:12:38.5	-470.1	4.5
HKPN 15	0:39:15.84	40:12:39.3	-482.9	5.3
HKPN 16	0:39:16.29	40:22:12.8	-526.1	5.6
HKPN 17	0:39:18.51	40:09:19.0	-376.3	4.1
HKPN 18	0:39:24.53	40:07:02.4	-434.4	2.7
HKPN 19	0:39:26.12	40:44:26.0	-373.1	27.7
HKPN 20	0:39:27.26	40:29:03.6	-532.4	12.6
HKPN 21	0:39:31.62	40:14:19.9	-510.4	3.6
HKPN 22	0:39:36.66	40:17:51.3	-503.8	3.4
HKPN 23	0:39:38.40	39:21:45.6	-394.5	8.8
HKPN 24	0:39:40.38	40:13:24.7	-454.4	3.1
HKPN 25	0:39:42.80	40:22:49.2	-490.9	8.0
HKPN 26	0:39:43.99	40:35:42.0	-465.7	12.1
HKPN 27	0:39:44.64	40:19:59.2	-500.1	3.1
HKPN 28	0:39:44.79	40:12:04.2	-472.0	6.5
HKPN 29	0:39:45.40	40:31:42.6	-538.9	4.6
HKPN 30	0:39:46.14	40:11:01.7	-416.1	2.1
HKPN 31	0:39:46.71	39:38:42.6	-573.1	3.2

Table 1—Continued

ID	RA (2000)	Dec (2000)	v_{helio}	v_{err}
HKPN 32	0:39:49.08	40:42:39.5	−168.8	28.6
HKPN 33	0:39:49.62	40:21:25.1	−396.2	4.0
HKPN 34	0:39:52.56	40:09:32.4	−481.1	6.4
HKPN 35	0:39:53.93	40:31:56.5	−442.7	24.6
HKPN 36	0:39:54.23	39:51:00.0	−486.0	3.3
HKPN 37	0:40:01.81	40:37:28.7	−552.4	10.6
HKPN 38	0:40:07.65	40:28:34.1	−457.4	5.3
HKPN 39	0:40:12.82	40:13:02.4	−387.3	4.3
HKPN 40	0:40:13.97	40:10:26.4	−504.0	2.3
HKPN 41	0:40:14.24	40:23:23.9	−126.1	2.5
HKPN 42	0:40:14.51	40:38:50.7	−513.4	12.2
HKPN 43	0:40:15.29	40:24:13.6	−472.9	4.4
HKPN 44	0:40:16.20	40:09:59.7	−447.9	6.9
HKPN 45	0:40:20.85	40:28:08.9	−506.0	2.9
HKPN 46	0:40:26.61	40:27:59.3	−472.2	26.9
HKPN 47	0:40:30.80	40:36:54.4	−482.6	2.6
HKPN 48	0:40:33.70	40:13:46.8	−295.0	4.7
HKPN 49	0:40:37.96	40:13:35.5	−578.9	3.3
HKPN 50	0:40:43.39	39:57:02.3	−423.4	2.7
HKPN 51	0:40:44.02	40:25:08.7	−528.2	36.7
HKPN 52	0:40:44.24	40:27:11.2	−485.8	6.1
HKPN 53	0:40:45.33	40:41:30.3	−524.9	5.1
HKPN 54	0:40:46.82	39:51:48.5	−418.1	6.9
HKPN 55	0:40:47.30	40:28:25.6	−479.4	7.7
HKPN 56	0:40:49.58	40:39:46.8	−416.1	18.7
HKPN 57	0:40:56.88	40:20:09.0	−560.5	3.9
HKPN 58	0:40:57.23	40:36:07.8	−498.2	8.6
HKPN 59	0:41:00.28	40:28:50.0	−425.2	2.4
HKPN 60	0:41:01.86	40:24:20.3	−421.1	23.5
HKPN 61	0:41:03.72	40:41:13.6	−556.1	6.0
HKPN 62	0:41:12.34	40:35:58.2	−528.4	10.0

Table 1—Continued

ID	RA (2000)	Dec (2000)	v_{helio}	v_{err}
HKPN 63	0:41:13.50	40:42:15.8	-526.7	14.0
HKPN 64	0:41:20.40	39:28:10.6	-274.0	13.8
HKPN 65	0:41:26.34	39:59:48.4	-448.2	17.7
HKPN 66	0:41:26.48	40:32:45.4	-399.6	4.0
HKPN 67	0:41:26.84	40:43:16.2	-394.0	14.1
HKPN 68	0:41:33.67	40:20:39.5	-396.6	3.8
HKPN 69	0:41:38.18	39:54:59.8	-413.5	2.3
HKPN 70	0:42:03.33	40:31:39.8	-539.0	4.0
HKPN 71	0:42:04.07	40:29:37.7	-513.8	26.7
HKPN 72	0:42:05.09	40:43:16.3	-449.4	44.3
HKPN 73	0:42:19.12	40:57:09.0	-281.5	8.7
HKPN 74	0:42:21.19	40:33:49.9	-379.7	4.2
HKPN 75	0:42:22.82	40:43:06.6	-509.1	6.9
HKPN 76	0:42:29.75	41:03:30.4	-451.3	5.4
HKPN 77	0:42:32.35	40:42:26.2	-362.2	8.6
HKPN 78	0:42:37.21	41:04:19.4	-461.1	8.0
HKPN 79	0:42:44.49	40:17:31.0	-458.9	3.7
HKPN 80	0:42:46.60	40:26:15.2	-462.8	3.9
HKPN 81	0:42:49.84	40:51:10.6	-505.7	10.0
HKPN 82	0:42:50.58	40:04:48.5	-477.6	4.5
HKPN 83	0:42:52.05	40:29:03.1	-261.1	20.1
HKPN 84	0:42:52.11	40:29:03.9	-294.1	2.6
HKPN 85	0:42:55.60	41:03:40.9	-599.1	5.6
HKPN 86	0:42:56.02	40:51:12.5	-638.3	5.3
HKPN 87	0:42:56.18	40:35:40.4	-534.8	8.6
HKPN 88	0:42:57.81	41:12:43.4	-199.2	18.0
HKPN 89	0:42:58.82	41:22:13.2	-142.5	4.6
HKPN 90	0:43:03.15	40:57:18.5	-367.4	11.0
HKPN 91	0:43:05.26	40:53:34.1	-532.3	4.8
HKPN 92	0:43:06.16	41:10:56.0	-337.9	3.9
HKPN 93	0:43:13.72	40:52:32.4	-381.5	6.0

Table 1—Continued

ID	RA (2000)	Dec (2000)	v_{helio}	v_{err}
HKPN 94	0:43:15.18	40:51:12.7	−500.3	6.2
HKPN 95	0:43:19.00	40:58:02.1	−452.0	4.3
HKPN 96	0:43:20.61	40:55:32.4	−309.9	11.2
HKPN 97	0:43:20.63	40:57:44.5	−502.8	12.0
HKPN 98	0:43:21.64	40:59:12.7	−388.8	28.8
HKPN 99	0:43:23.00	41:15:40.4	−251.3	10.0
HKPN 100	0:43:28.32	40:51:19.9	−433.9	25.2
HKPN 101	0:43:36.79	41:03:33.4	−260.3	7.4
HKPN 102	0:43:36.80	40:37:38.6	−323.9	12.4
HKPN 103	0:43:44.52	40:59:59.7	−274.7	4.3
HKPN 104	0:44:04.65	41:12:08.9	−293.0	4.7
HKPN 105	0:44:04.94	41:09:18.6	−212.8	13.7
HKPN 106	0:44:07.49	41:10:09.7	−270.6	6.4
HKPN 107	0:44:08.01	40:03:13.6	−391.4	3.8
HKPN 108	0:44:11.42	41:01:02.2	−348.6	6.0
HKPN 109	0:44:11.92	41:14:00.0	−232.4	4.5
HKPN 110	0:44:15.88	41:22:10.4	−251.2	5.0
HKPN 111	0:44:21.04	41:15:41.1	−281.8	4.2
HKPN 112	0:44:25.50	40:14:36.6	−428.5	8.0
HKPN 113	0:44:25.98	40:15:45.7	−350.4	3.2
HKPN 114	0:44:30.33	40:07:29.5	−425.7	2.3
HKPN 115	0:44:37.91	41:14:14.4	−219.3	15.0
HKPN 116	0:44:37.97	41:07:02.9	−335.9	11.7
HKPN 117	0:44:42.22	41:08:01.8	−243.5	4.9
HKPN 118	0:44:42.77	40:40:05.7	−383.8	4.7
HKPN 119	0:44:43.80	41:14:28.0	−315.7	5.9
HKPN 120	0:44:50.69	41:17:22.3	−288.6	5.3
HKPN 121	0:44:53.16	41:15:58.0	−306.6	28.5
HKPN 122	0:44:54.43	40:52:45.4	−453.7	3.8
HKPN 123	0:44:54.98	41:09:53.2	−321.1	5.1
HKPN 124	0:44:56.30	41:20:25.4	−296.6	4.5

Table 1—Continued

ID	RA (2000)	Dec (2000)	v_{helio}	v_{err}
HKPN 125	0:45:05.05	41:12:52.5	–201.0	10.9
HKPN 126	0:45:05.30	41:09:38.6	–278.5	6.3
HKPN 127	0:45:07.14	40:39:33.4	–285.8	7.7
HKPN 128	0:45:28.36	41:04:54.2	–400.5	16.8
HKPN 129	0:45:35.32	40:59:57.2	–205.1	9.4
HKPN 130	0:45:38.13	40:59:19.5	–279.0	10.9
HKPN 131	0:47:00.98	40:49:23.4	–350.5	3.1
HKPN 132	0:48:22.14	40:45:41.9	–320.0	3.4
HKPN 133	0:48:24.78	41:08:11.1	–353.2	3.3
HKPN 134	0:48:27.23	39:55:34.0	–186.8	2.4
HKPN 135	0:49:28.30	40:59:54.0	–242.6	3.4

Table 2. PN candidates in M32.

ID	$\alpha(2000)$	$\delta(2000)$	v_{helio}	v_{err}
1	0:42:23.24	40:46:28.7	-182.4	8.4
2	0:42:28.93	40:44:39.0	-158.3	6.6
3	0:42:40.10	40:49:41.3	-160.5	3.6
4	0:42:40.24	40:51:03.0	-149.6	2.3
5	0:42:50.63	40:45:28.4	-183.7	2.3
6	0:42:53.02	40:48:59.8	-213.5	2.0
7	0:42:56.97	40:51:01.8	-169.1	24.8
8	0:43:02.04	40:49:30.2	-154.6	4.7

Table 3. HII Regions in And IV

ID	$\alpha(2000)$	$\delta(2000)$	v_{helio}	v_{err}
6	0:42:30.57	40:34:46.9	270.2	39.2
3	0:42:32.17	40:33:58.7	233.0	3.4
4	0:42:31.73	40:34:11.2	249.5	5.2

^aID numbers correspond to those given in Ferguson et al. (2000).

Table 4: Kinematic Models

Model	h_r kpc	h_z kpc	v_{rot} km/s	Density Distribution	σ_r km/s	σ_ϕ, σ_z km/s
thin	5.9	0.3	230	$L(R, z) = e^{(-R/h_r)} e^{(-z/h_z)}$	$\sigma_r = \sqrt{h_z} v_{circ} e^{-R/2h_r}$	$(\sigma_\phi, \sigma_z) = (\frac{\sigma_r}{\sqrt{2}}, \frac{\sigma_r}{2})$
thick	5.9	1.0	230	$L(R, z) = e^{(-R/h_r)} e^{(-z/h_z)}$	$\sigma_r = \sqrt{h_z} v_{circ} e^{-R/2h_r}$	$(\sigma_\phi, \sigma_z) = (\frac{\sigma_r}{\sqrt{2}}, \frac{\sigma_r}{2})$
bulge	2.4	...	150	$L(R, z) = e^{-7.67((-R/R_e)^{1/4}-1)}$	$\sigma_r = constant$	$\sigma_\phi = \sigma_z = \sigma_r$

Table 5. Milky Way Disk Properties.

Population	h_r	h_z	v_{circ}	σ_r
Milky Way thin	3.5	.3	-220	30
Milky Way thick	4	1.0	-220	65

Table 6. Coordinates and heliocentric velocities for Halo PN candidates in M31.

ID	RA (2000)	Dec (2000)	v_{helio}	v_{err}
HKPN 86	0:42:56.02	40:51:12.5	−638.3	5.3
HKPN 85	0:42:55.60	41:03:40.9	−599.1	5.6
HKPN 32	0:39:49.08	40:42:39.5	−168.8	28.6
HKPN 41	0:40:14.24	40:23:23.9	−126.1	2.5
NF	0:46:26.51	43:00:42.15	−452.3	...

Note. — The last object is from the study of Nolthenius & Ford 1987.